A&A 491, 363–377 (2008)
DOI: 10.1051/0004-6361:200810122


Astronomy & Astrophysics

# Suzaku broad-band spectroscopy of RX J1347.5–1145: constraints on the extremely hot gas and non-thermal emission

N. Ota[1,2,⋆], K. Murase[3], T. Kitayama[4], E. Komatsu[5], M. Hattori[6], H. Matsuo[7], T. Oshima[8], Y. Suto[9], and K. Yoshikawa[10]

[1] Max-Planck-Institut für extraterrestrische Physik, Giessenbachstraße, 85748 Garching, Germany
e-mail: ota@mpe.mpg.de
[2] Institute of Space and Astronautical Science, Japan Aerospace Exploration Agency, 3-1-1 Yoshinodai, Sagamihara, Kanagawa 229-8510, Japan
[3] Saitama University, Shimo-Okubo 255, Sakura, Saitama 338-8570, Japan
[4] Toho University, 2-2-1 Miyama, Funabashi, Chiba 274-8510, Japan
[5] The University of Texas at Austin, 2511 Speedway, RLM 15.306, Austin, TX 78712, USA
[6] Tohoku University, Aramaki, Aoba, Sendai 980-8578, Japan
[7] National Astronomical Observatory of Japan, 2-21-1 Osawa, Mitaka, Tokyo 181-8588, Japan
[8] Nobeyama Radio Observatory, Minamimaki, Minamisaku, Nagano 384-1805, Japan
[9] The University of Tokyo, Tokyo 113-0033, Japan
[10] Center for Computational Physics, University of Tsukuba, Tsukuba, Ibaraki 305-8577, Japan

Received 5 May 2008 / Accepted 28 August 2008

**ABSTRACT**

*Context.* We present the results of our analysis of long Suzaku observations (149 ks and 122 ks for XIS and HXD, respectively) of the most X-ray luminous galaxy cluster, RX J1347.5–1145, at $z = 0.451$.
*Aims.* To understand the gas physics of a violent, cluster merger, we study physical properties of the hot (∼20 keV) gas clump in the south-east (SE) region discovered previously by Sunyaev–Zel'dovich (SZ) effect observations. Using hard X-ray data, a signature of non-thermal emission is also explored.
*Methods.* We perform single as well as multi-temperature fits to the Suzaku XIS spectra. The Suzaku XIS and HXD, and the Chandra ACIS-I data are then combined to examine the properties of the hot gas component in the SE region. We finally look for non-thermal emission in the Suzaku HXD data.
*Results.* The single-temperature model fails to reproduce the 0.5–10 keV continuum emission and Fe-K lines measured by XIS simultaneously. A two-temperature model with a very hot component improves the fit, although the XIS data can only provide a lower limit to the temperature of the hot component. In the Suzaku HXD data, we detect hard X-ray emission above the background in the 12–40 keV band at the $9\sigma$ level; however, the significance becomes marginal when the systematic error in the background estimation is included. With the joint analysis of the Suzaku and Chandra data, we determine the temperature of the hot gas in the SE region to be $25.3^{+6.1}_{-4.5}$ (statistical; 90% confidence level) $^{+6.9}_{-9.5}$ (systematic; 90% confidence level) keV, which is in an excellent agreement with the previous joint analysis of the SZ effect in radio and the Chandra X-ray data. This is the first time that the X-ray analysis alone provides a good measurement of the hot component temperature in the SE region, which is possible because of Suzaku's unprecedented sensitivity over the wide X-ray band. These results indicate strongly that RX J1347.5–1145 has undergone a recent, violent merger. The spectral analysis shows that the SE component is consistent with being thermal. We measure the $3\sigma$ upper limit to the non-thermal flux, $F < 8 \times 10^{-12}$ erg s$^{-1}$ cm$^{-2}$ in the 12–60 keV band, which provides a limit on the inverse Compton scattering of relativistic electrons off the CMB photons. Combining this limit with the discovery of a radio mini halo in this cluster at 1.4 GHz, which measures the synchrotron radiation, we find a lower limit to the strength of the intracluster magnetic field, such that $B > 0.007$ $\mu$G.

**Key words.** galaxies: clusters: individual: RX J1347.5-1145 – galaxies: intergalactic medium – X-rays: galaxies: clusters – cosmology: observations

## 1. Introduction

RX J1347.5–1145 is one of the most extensively studied distant clusters of galaxies, located at $z = 0.451$, which is also known as the most X-ray luminous cluster of galaxies on the sky. The bolometric luminosity of RX J1347.5–1145 is $L_{\rm X,bol} \sim 2 \times 10^{46}$ erg s$^{-1}$ (Schindler et al. 1997).

The previous multi-wavelength observations have shown that RX J1347.5–1145 has an unusually violent merger activity, which makes this cluster an ideal target for probing the intracluster gas physics and non-thermal phenomena associated with the cluster merger at high redshifts.

The global temperature of the intracluster medium (ICM) of RX J1347.5–1145 is as high as 9–14 keV, as indicated from observations with several X-ray satellites (Schindler et al. 1997; Ettori et al. 2001; Allen et al. 2002; Gitti et al. 2007b). This cluster was classified as a "cooling-flow" cluster because of its centrally peaked X-ray surface brightness profile as well as its high mass accretion rate estimated at the center (Schindler et al. 1997; Allen et al. 2002).

⋆ Research fellow of the Alexander von Humboldt Foundation.

**Table 1.** Log of *Suzaku* observations of RX J1347.5–1145.

| Target | Sequence No. | Date | Coordinates[a] | | Exposure [s][b] | |
|---|---|---|---|---|---|---|
| | | | RA [deg] | Dec [deg] | XIS | PIN |
| RXJ1347.5–1145 | 801013010 | 2006 June 30 | 206.8560 | −11.8093 | 69 661 | 56 698 |
| RXJ1347.5–1145 | 801013020 | 2006 July 15 | 206.8558 | −11.8095 | 79 126 | 64 922 |

[a] Pointing coordinates in J2000; [b] net exposure time after data filtering.

The most striking feature of RX J1347.5–1145 is the presence of an extremely hot, ∼20 keV, gas clump in the south-east (SE) region. This component was discovered by radio observations of the Sunyaev-Zel'dovich (SZ) effect towards RX J1347.5–1145 at 150 GHz as the prominent substructure of the SZ effect in the SE region, about 20″ off at its the center (Komatsu et al. 2001). Kitayama et al. (2004) performed a detailed joint analysis of the SZ effect decrement data at 150 GHz (Komatsu et al. 2001), increment data at 350 GHz (Komatsu et al. 1999), and the *Chandra* ACIS-S3 X-ray data (Allen et al. 2002), and determined the temperature of the hot gas clump to be in excess of 20 keV, which is much higher than the average temperature of the ambient gas.

The coexistence of the cool and hot ICM in the central region indicates a complex dynamical evolution of the system, such as a recent merger. In the optical band, the cluster center is dominated by two cD galaxies. The dark matter distribution has also been studied by the gravitational lensing effect (e.g. Fischer & Tyson 1997; Sahu et al. 1998; Cohen & Kneib 2002; Allen et al. 2002; Bradač et al. 2008; Miranda et al. 2008; Halkola et al. 2008). An elongated, almost bimodal distribution was found (Bradač et al. 2008), which also implies that a cluster merger has occurred. Another line of evidence for a merger is the discovery of a radio mini halo at the cluster center (Gitti et al. 2007a), which suggests the presence of relativistic particles powered by the merger and the cooling flow.

The X-ray data from the *ROSAT* satellite (Schindler et al. 1997) failed to identify the hot component in the SE region, because its X-ray sensitivity did not extend to such a high temperature. RX J1347.5–1145 was considered to be a *relaxed*, non-merging cluster until the SZ effect revealed evidence of a violent merger. This example shows the importance of having sensitivity to high temperatures well in excess of 10 keV.

Such a high temperature component appears normal in merging clusters. Another, perhaps the most famous, example is the Bullet cluster (1E0657-56), in which hot gas substructure was also found (Markevitch et al. 2002). The analysis of the temperature structure in merging clusters is a powerful tool for understanding the gas physics in extreme conditions. While X-ray spectroscopy has been used widely in this type of study, it is not easy to measure precisely the temperature of very hot ($kT \gg 10$ keV) gas, since the majority of X-ray imaging spectroscopic observations are limited to the energy band below 10 keV, and therefore cannot measure a spectral cut-off at $kT$ that is characteristic of the thermal bremsstrahlung emission.

To overcome this difficulty, Kitayama et al. (2004) used the fact that the SZ effect is sensitive to arbitrary high temperature gas, and performed a joint analysis of the SZ effect and X-ray images. They determined the temperature of the SE excess component in RX J1347.5–1145 to be $28 \pm 7$ keV, while the *Chandra* X-ray spectroscopy, whose sensitivity degrades significantly beyond 7 keV, provided a lower limit of 22 keV. This is amongst the hottest gas detected to date. Based on the numerical simulations by Takizawa (1999), Kitayama et al. (2004) suggested that RX J1347.5–1145 had experienced a recent merger at the collision speed of 4500 km s$^{-1}$, which is similar to that measured for the Bullet cluster (Milosavljević et al. 2007; Springel & Farrar 2007; Mastropietro & Burkert 2007; Nusser 2008). This result indicates that RX J1347.5–1145 is almost identical to the Bullet cluster, except for its viewing angle.

The conclusion of Kitayama et al. (2004) was based on SZ data from high-resolution mapping observations of the SZ effect (the highest resolution ever achieved to date; Komatsu et al. 1999, 2001). However, the precision of these SZ observations is still limited because of technological reasons; thus, high-precision X-ray observations whose sensitivity goes well beyond 10 keV are required to obtain reliable estimates of physical properties, such as temperature and merging velocity.

The unprecedented sensitivity of the *Suzaku* satellite (Mitsuda et al. 2007) to hard X-ray emission well over 10 keV offers a wonderful opportunity to study violent merger events. In this paper, we present an analysis of the temperature structure and non-thermal, high-energy component of the distant cluster RX J1347.5–1145 with the onboard instruments, the X-ray Imaging Spectrometer (XIS; Koyama et al. 2007), and the Hard X-ray Detector (HXD; Takahashi et al. 2007; Kokubun et al. 2007). These instruments provide high-sensitivity spectroscopic observations in a wide energy band up to several tens of keV. Combined with the *Chandra* data, we determine the temperature of the SE clump *only from the X-ray spectroscopy*, and discuss its physical properties. We also constrain, for the first time, the non-thermal hard X-ray emission and estimate the magnetic-field strength in RX J1347.5–1145.

Throughout this paper, we adopt a cosmological model with the matter density $\Omega_{\rm M} = 0.27$, the cosmological constant $\Omega_\Lambda = 0.73$, and the Hubble constant $H_0 = 72$ km s$^{-1}$ Mpc$^{-1}$, which are consistent with the WMAP 5-year results (Dunkley et al. 2008; Komatsu et al. 2008). At the cluster redshift ($z = 0.451$), 1″ corresponds to 5.74 kpc. Unless otherwise specified, quoted errors indicate the 90% confidence intervals.

## 2. Observation and data reduction

Long observations of RX J1347.5–1145 were completed twice in the *Suzaku* AO-1 period. During the observations, XIS and HXD were operated in their normal modes. To prioritize the HXD effective area, the target was observed at the HXD nominal aimpoint (i.e. 3′.5 off-axis relative to the XIS). The total exposure time after data filtering was 149 ks/122 ks for XIS/HXD. The summary of observations is given in Table 1.

The XIS consists of four X-ray CCD cameras: three front-illuminated CCDs (XIS-0, –2, –3: 0.4–12 keV) and one back-illuminated CCD (XIS-1: 0.2–12 keV), and covers a field of view of 18′ × 18′. The "Spaced Charge Injection" option was not applied. The energy resolution was ∼160 eV at 6 keV (FWHM) at the time of observations. As shown in Fig. 1, the X-ray emission from the cluster is clearly detected. The X-ray peak position (13:47:30.3, −11:45:00.9) is consistent with that derived from *Chandra* observations (13:47:30.6, −11:45:09.3) and

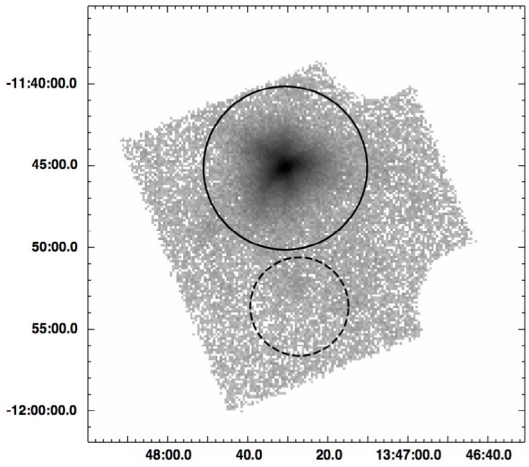


**Fig. 1.** *Suzaku* XIS-0 image of RX J1347.5–1145 in the 0.5–10 keV band. The spectral integration regions for the cluster and the background are indicated with the solid and dashed circles, respectively. The two corners of the CCD chip illuminated by $^{55}$Fe calibration sources are excluded from the image.

within the accuracy of the attitude determination of *Suzaku* (typically <20″; Uchiyama et al. 2008).

The non-imaging HXD covers a wide bandpass of 10–600 keV with PIN diodes (10–60 keV) and GSO scintillator (40–600 keV). We used the PIN data in the analysis presented in this paper. The narrow field-of-view of ∼30′ × 30′ (*FWHM*) and the low background level of the PIN spectral data enabled us to study the hard X-ray emission from the cluster up to several tens of keV, which is ideal for studying a violent merger event. The bias voltage from one of four high-voltage units was reduced from the nominal value of 500 V to 400 V. As a result the total effective area of the HXD/PIN decreased by a few percent to just above 20 keV. This effect was incorporated into the detector response functions.

We used the cleaned event files created by the pipeline processing version 2.0, and performed the data analysis using `HEASOFT` version 6.3.1. The XIS data was filtered according to the following criteria: the Earth elevation angle >10°, the day-Earth elevation angle >20°, and the satellite outside the South Atlantic Anomaly (SAA). The HXD data were filtered according to the following criteria: the Earth elevation angle >5°, the geomagnetic cut-off rigidity (COR) > 6 GV, and the satellite outside the SAA.

The XIS spectra were extracted from a circular region within a radius of 5′ that is centered at the X-ray peak position (see Fig. 1). The background spectra were accumulated from the circular region within a 3′ radius which is almost entirely free of cluster emission. Since the background contributes to 10–15% of the total spectrum continuum level, the systematic error due to the background uncertainty is small. To confirm this, we checked the positional dependence of the background spectra by analyzing the blank-sky data obtained during the ∼90 ks North Ecliptic Pole observation on 2006 February 10, and found that it was lower than 7% of the background spectrum continuum level for all four sensors of XIS. Therefore, the background does not affect our spectral analysis within the statistical errors.

The energy response files were generated by using the `FTOOLS` task, `xisrmfgen`. To take into account the vignetting effect of the X-ray telescopes (XRT; Serlemitsos et al. 2007) and a decrease in the low-energy efficiency due to the contaminating material on the optical blocking filter of the XIS, the auxiliary response files (arfs) were calculated by using `xissimarfgen` (Ishisaki et al. 2007). We assumed that the X-ray surface brightness distribution of the cluster was represented by the double $\beta$-model: our reanalysis of the *Chandra* ACIS-I image yields the two core radii given by $r_{c1} = 24$ kpc and $r_{c2} = 94$ kpc, the same slope parameter, $\beta = 0.63$, for both components, and a surface brightness ratio of $S_1/S_2 = 8.1$ at the center (see Fig. 9b). Since the spatial distribution of RX J1347.5–1145 is compact compared with the typical size of the *Suzaku's* Point Spread Function (PSF), its detailed features do not affect our spectral analysis significantly: if we compare the above arf files with those produced by using a point-like source or an exposure-corrected *Chandra* image as an input source distribution, these three kinds of arfs agree to within 3%, and provide consistent spectral parameters to within the present calibration uncertainty of the *Suzaku* telescope (see also Appendix A).

The hard X-ray spectra were accumulated from all units of the PIN diodes. The PIN detector background was subtracted by using the Non-X-ray Background (NXB) files[1] provided by the HXD instrument team. Since precise modeling of the background is crucial for measuring the hard X-ray flux, we describe the method of background subtraction in Sect. 4. In the spectral fitting, we used the PIN response function[2] that was appropriate for the epoch of observations.

## 3. XIS analysis: 0.5–10 keV

To examine the global temperature structure of RX J1347.5–1145, we attempted to reproduce the observed XIS spectra in the 0.5–10 keV band by fitting the APEC thermal emission model.

The angular size of the X-ray emission is fairly compact and nearly 90% of the total emission originates in the central $r < 2'$ region, which is comparable to the spatial resolution of the *Suzaku* XRT (Half Power Diameter ∼2′; Serlemitsos et al. 2007). We use the extraction radius of 5′; more than 97% of the photons from RX J1347.5–1145 have therefore been collected.

### 3.1. Fitting with the single-temperature model

The XIS spectra with high photon statistics allowed us to measure the global temperature in two different ways: (1) by a APEC model fit to the 0.5–10 keV spectra; and (2) by using the intensity ratio of two Fe emission lines, i.e. (He-like Fe K$\alpha$)/(H-like Fe K$\alpha$), as an indicator of the "ionization" temperature. By comparing the two results of these methods, we examined whether the emission could be modeled by a single-temperature gas, or the data had to be described instead by a model of more complex temperature structure.

For the analysis (1) (APEC model), we fitted the APEC model to the observed 0.5–10 keV XIS spectra, where the redshift and Galactic hydrogen column density were fixed at $z = 0.451$ and $N_{\rm H} = 4.85 \times 10^{20}$ cm$^{-2}$ (Dickey & Lockman 1990), respectively. The metal abundance table in Anders & Grevesse (1989) was assumed. The spectral bins in the 1.7–1.9 keV range were excluded due to the large calibration errors in the Si-edge structure. To take into account the uncertainty in the thickness of the contaminating material, the absorption column densities of oxygen and carbon ($N_{\rm C}$ and $N_{\rm O}$) were included in the spectral model by fixing the ratio to $N_{\rm C}/N_{\rm O} = 6$. There was a potential uncertainty in the absolute energy scale of approximately

[1] http://www.astro.isas.jaxa.jp/suzaku/analysis/hxd/pinnxb/pinnxb_ver2.0/

[2] ae_hxd_pinhxnome2_20070914.rsp

10–20 eV, as indicated by the analysis of the $^{55}$Fe calibration source spectra; the gain offset for each XIS sensor was therefore included in the fitting model.

Since all four sensors yield consistent APEC parameters (see Table 2), we show the results from the simultaneous fit to all of the sensors (XIS-0, XIS-1, XIS-2, and XIS-3) hereafter. When performing the simultaneous fit, the normalizations of XIS-1, XIS-2, and XIS-3 relative to that of XIS-0 were also treated as free parameters. We find the temperature and the metal abundance of $kT = 12.86^{+0.08}_{-0.25}$ keV and $Z = 0.33^{+0.03}_{-0.02}$ solar, respectively. The unabsorbed flux and luminosity in the 0.5–10 keV band are $F_{\rm X,0.5-10\,keV} = 1.3 \times 10^{-11}$ erg s$^{-1}$ cm$^{-2}$, and $L_{\rm X,0.5-10\,keV} = 8.7 \times 10^{45}$ erg s$^{-1}$, respectively. The estimated bolometric X-ray luminosity is $L_{\rm X,bol} = 1.37 \times 10^{46}$ erg s$^{-1}$. In Table 3, we list the instrumental calibration parameters. In the following analysis, we use the best-fit values for the relative normalization factors, the carbon column densities, and the gain offsets.

Figure 2 shows the observed XIS spectra. Figure 2b is a zoomed version of this figure for the region around the redshifted He-like Fe K$\alpha$ and H-like Fe K$\alpha$ lines at about 4.6 keV and 4.8 keV, respectively. We find clear detections of both lines. Also shown is the best-fit single-temperature APEC thermal plasma model. The single-temperature model fails to reproduce the He-like line. The reduced $\chi^2$ from the single-temperature fit is $\chi^2 = 1320.4/1198$; the single-temperature model is therefore rejected at the 99.3% confidence level.

We then attempted to fit the XIS spectra with the NEI (non-equilibrium ionization collisional plasma) model. We found that the NEI model did not improve the fit to the He-like Fe K$\alpha$ line and the quality of the fit in the entire energy range was similar to the 12.9 keV APEC model: the resulting $\chi^2$ from the NEI model fit was 1340 for 1208 degrees of freedom. The best-fit ionization timescale of $>10^{12}$ s cm$^{-3}$ is also long sufficiently for the system to reach the equilibrium state (Masai 1994), and the assumption that the system is in a non-equilibrium state cannot therefore be justified. From these results, we conclude that the single-temperature NEI model fails to describe the observed XIS spectra.

For the analysis (2) (the line-ratio method), we model the observed XIS spectra in the 4–5.5 keV band as the sum of the following components: (i) the APEC model with the metal abundance reset to 0 for the continuum emission; (ii) two Gaussian functions for the two major Fe lines at 4.6 and 4.8 keV; and (iii) another Gaussian line at 5.4 keV for the blend of the He-like Ni-K$\alpha$ and He-like Fe-K$\beta$ lines. In Fig. 3a, we show the results of this fit. This model provides an acceptable fit to the data with $\chi^2$/d.o.f. = 185/163, or a probability of finding higher $\chi^2$ values than observed is 11.4%.

This model provides the line ratio, (He-like Fe K$\alpha$)/(H-like Fe K$\alpha$), of 1.05(0.92–1.34). Figure 3b shows the temperature dependence of the line ratio predicted by the APEC model, folded with the XRT+XIS response functions. From this, we find $kT = 10.4(9.1–11.4)$ keV, which is significantly different from that found in the analysis (1), $kT = 12.86(12.61–12.94)$ keV, suggesting that the ICM cannot be explained by the single-temperature model. Therefore, the ICM is more likely to be in the form of multi-temperature plasma, which we explore in Sect. 3.2.

Since the iron lines are emitted mostly from low-temperature gas (see Sect. 3.2), the line energies and widths are useful probes of (i) the gas bulk motion; and (ii) the turbulence in the cluster core. For (i), the observed centroid energies of the iron lines are consistent with those expected from the 10 keV APEC model (6.69 and 6.97 keV in the rest frame) and the cluster redshift, to within the 90% statistical error of 10 eV. As shown in Table 3, there is the gain offset of 15 eV when averaged over the four XIS sensors, and we simply assign the 90% systematic error of 15 eV to the XIS energy scale. By adding the statistical and systematic errors in quadrature, the 90% upper limit to the line-of-sight bulk velocity relative to $z = 0.451$ is estimated to be $\Delta V < 1200$ km s$^{-1}$. For (ii), we find no significant line broadening: the 90% upper limit to the Gaussian width of the He-like K$\alpha$ line is measured to be $\sigma_{\rm measured} < 35$ eV. Since the measured Gaussian width is the sum of the thermal Doppler broadening, $\sigma_0$ ($\sigma_0 = 4$ eV for $kT = 10$ keV), and the broadening due to a turbulent velocity, $\sigma_{\rm turb}$, i.e. $\sigma^2_{\rm measured} = \sigma^2_0 + \sigma^2_{\rm turb}$, an upper limit to the turbulent velocity dispersion is measured to be $\sigma_{\rm turb} < 1500$ km s$^{-1}$. Therefore, from the analysis of the iron lines we found no significant bulk velocity and turbulent velocity, which is consistent with the view that the low-temperature gas in the cluster core is relatively relaxed. The derived upper limits are also comparable to those obtained for the core of the Centaurus cluster (Ota et al. 2007). If velocity structure on small ($<2'$) spatial scales exists, the signals may be diluted due to the wide PSF of *Suzaku*. However, it is not easy to study the detailed spatial structure in RX J1347.5–1145 because its angular size is small.

### 3.2. Fitting the two-temperature model

Given that the single-temperature model failed to describe the observed XIS spectra, we explored the two-temperature model consisting of two APEC models with different temperatures, as a simplest example of multi-temperature plasma. The results of the fit to the two-temperature model are shown in Fig. 4 and Table 4, where the metal abundances of the two components are assumed to be equal.

From the fit to the 0.5–10 keV spectra, we found that the low-temperature component had the temperature of $kT_{\rm low} = 9.7^{+0.7}_{-1.1}$ keV[3], whereas we only found a lower bound to the temperature of the high-temperature component as $kT_{\rm high} > 33$ keV. This two-temperature model yielded an acceptable goodness-of-fit: the reduced $\chi^2$ was $\chi^2 = 1295.0/1207$, or the probability of finding higher $\chi^2$ values than observed was 3.9%. In comparison with the single-temperature APEC model, the fit has improved to a confidence level of more than the 99.99% according to the F-test ($\Delta\chi^2 = 25$ for two additional parameters). Restricting the energy range to 4.0–5.5 keV did not change the parameters significantly (see the lower row of Table 4). The reduced $\chi^2$ is $\chi^2 = 185.2/159$, or the probability of finding higher $\chi^2$ values than observed was 7.6%.

Since the observed Fe K$\alpha$ lines should be totally dominated by the low-temperature gas (see Fig. 4b), one may compare $kT_{\rm low} = 9.7^{+0.7}_{-1.1}$ keV and the temperature derived from the line ratio, $kT = 10.4(9.1–11.4)$ keV (see Sect. 3.1), directly. These two estimates were in an excellent agreement, which provides support to the two-temperature interpretation of the ICM of RX J1347.5–1145.

Although the XIS data provide a lower bound to the temperature of the hotter component (see Table 4), they cannot provide an upper bound. We found that this was because the two-temperature model is too simple to be realistic. More detailed

[3] The temperature of the low-temperature component is similar to the temperature determined from the spectra taken by the GIS detectors onboard *ASCA* with the single-temperature model, $kT_{ASCA} = 9.3^{+1.1}_{-1.0}$ keV (Schindler et al. 1997).

**Table 2.** Single-temperature APEC model parameters fit to the XIS spectra taken by four sensors (XIS-0, XIS-1, XIS-2, XIS-3), and the result from the simultaneous fit to all of the sensors (XIS-0, 1, 2, 3).

| Sensor | $kT$ [keV] | $Z$ [solar] | $K^a$ | $\chi^2$/d.o.f. |
|---|---|---|---|---|
| XIS-0 | 13.31(12.76–13.86) | 0.35(0.28–0.40) | $1.37(1.37–1.39)\times10^{-2}$ | 352.1/298 |
| XIS-1 | 12.23(11.54–12.83) | 0.36(0.30–0.41) | $1.41(1.39–1.44)\times10^{-2}$ | 345.0/298 |
| XIS-2 | 12.87(12.40–13.32) | 0.34(0.29–0.38) | $1.40(1.38–1.42)\times10^{-2}$ | 316.5/298 |
| XIS-3 | 12.76(12.28–13.24) | 0.30(0.25–0.35) | $1.45(1.43–1.47)\times10^{-2}$ | 300.2/298 |
| XIS-0,1,2,3 | 12.86(12.61–12.94) | 0.33(0.31–0.36) | $1.37(1.36–1.39)\times10^{-2}$ | 1320.4/1198 |

[a] The APEC normalization, $K = \int n_e n_H dV/(4\pi D_A^2(1+z)^2)$ [$10^{14}$ cm$^{-5}$].

**Table 3.** The instrumental calibration parameters from the APEC model fit simultaneously to the XIS-0, 1, 2, and 3.

| Sensor | Relative normalization | $N_c$ $[10^{18}\mathrm{cm}^{-2}]$ | Gain offset [eV] |
|---|---|---|---|
| XIS-0 | 1(Fix) | 0.012(<0.116) | −12.0 (−20.0–−6.0) |
| XIS-1 | 1.035(1.023–1.047) | 0.093(0.014–0.184) | −16.0 (−22.5–−10.2) |
| XIS-2 | 1.019(1.007–1.030) | 0.011(<0.116) | −9.8 (−16.5–−3.1) |
| XIS-3 | 1.049(1.038–1.060) | 0.000(<0.100) | −20.1 (−26.4–−14.2) |

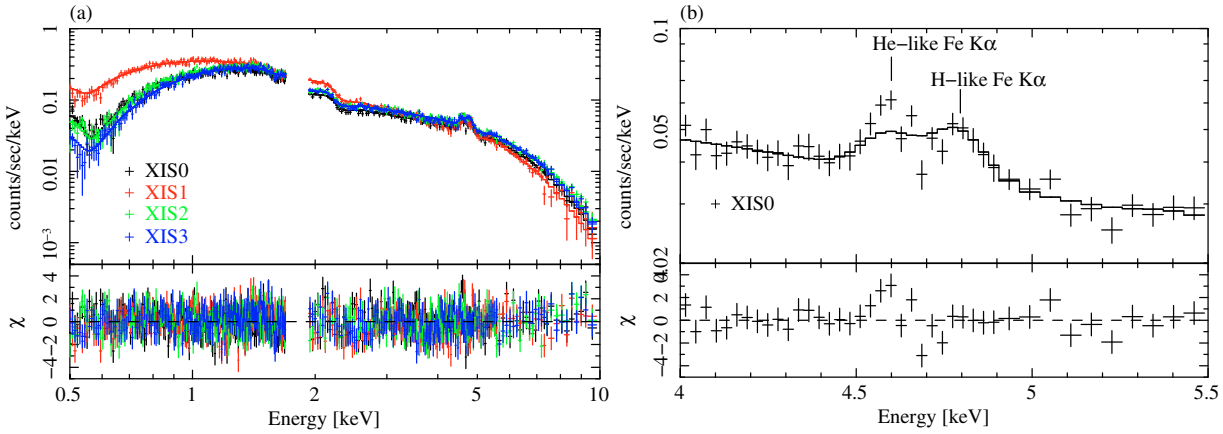


**Fig. 2. a)** Observed XIS spectra ($r < 5'$). The spectra taken by four sensors, XIS-0 (black), 1 (red), 2 (green), and 3 (blue), are shown separately. The solid lines in *the upper panel* show the best-fitting single-temperature APEC thermal plasma model simultaneously fit to all of the sensors, convolved with the telescope and the detector response functions. In *the bottom panel* the residuals of the fit in units of the number of standard deviations are shown. **b)** Blow-up of the XIS-0 spectrum in the 4–5.5 keV band. The single-temperature model fails to fit the He-like Fe K$\alpha$ line.

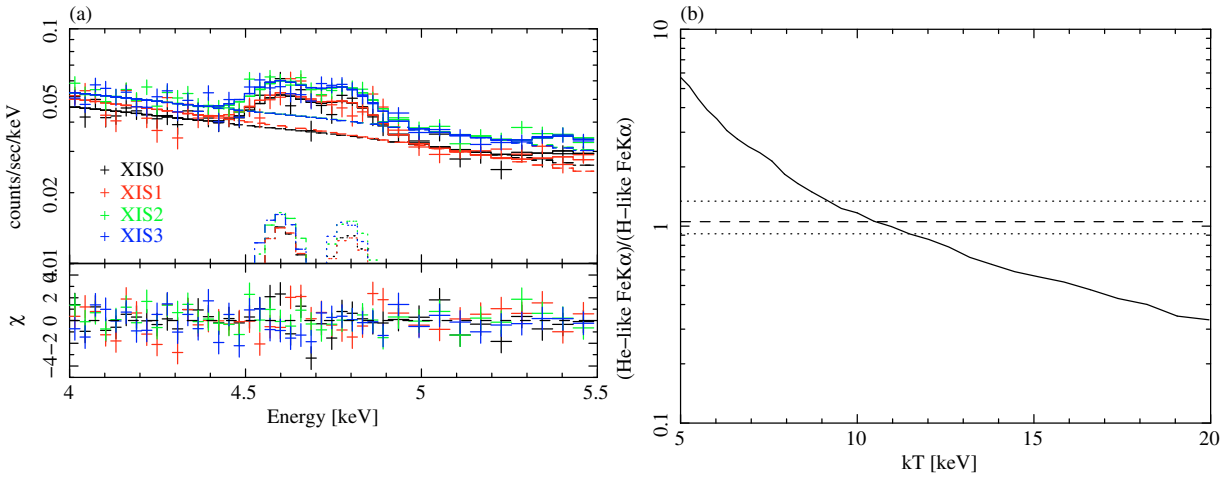


**Fig. 3. a)** Observed XIS spectra in the 4–5.5 keV band. The spectra taken by four sensors, XIS-0 (black), 1 (red), 2 (green), and 3 (blue), are shown separately. The solid lines in *the upper panels* are the best-fitting continuum plus two Gaussian models. In *the bottom panel* the residuals of the fit in units of the number of standard deviations are shown. **b)** Line ratio (He-like Fe K$\alpha$)/(H-like Fe K$\alpha$) as a function of temperature, calculated from the APEC model. The horizontal dashed line and the dotted lines show the best-fitting line ratio and the 90% confidence interval, respectively.

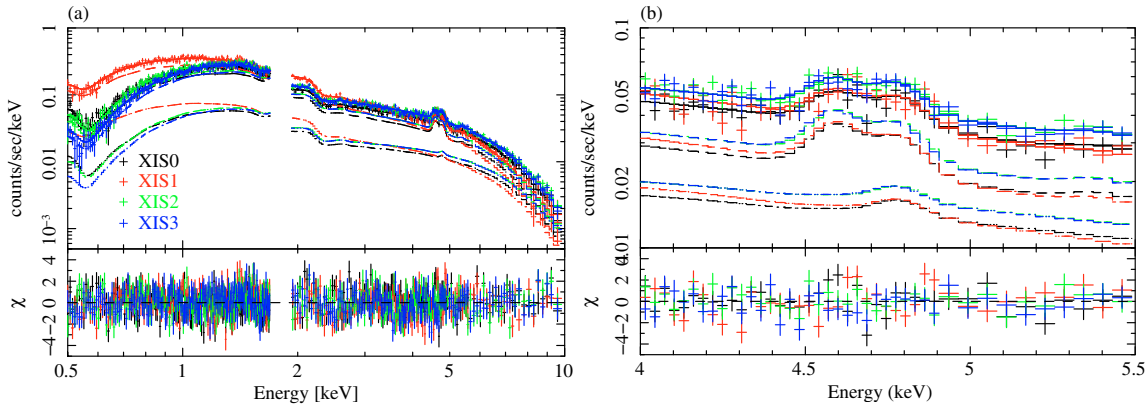


**Fig. 4. a)** Two-temperature APEC model fit to the observed XIS spectra. The spectra taken by four sensors, XIS-0 (black), 1 (red), 2 (green), and 3 (blue), are shown separately. The solid lines in *the upper panel* show the sum of two APEC models with different temperatures, while the dashed lines show the low-temperature (upper curves) and high-temperature (lower curves) components separately, convolved with the telescope and the detector response functions. In *the bottom panel* the residuals of the fit in units of the number of standard deviations are shown. **b)** Blow-up of the XIS spectra in the 4–5.5 keV band. The two-temperature model fits both the He-like and H-like Fe K$\alpha$ lines adequately.

**Table 4.** Two-temperature APEC model parameters fit to the XIS spectra in the 0.5–10 keV and 4.0–5.5 keV bands.

| Energy band | $i$ | $kT_i$ [keV] | $Z_i$ [solar] | $K_i$ | $\chi^2$/d.o.f. |
|---|---|---|---|---|---|
| 0.5–10 keV | 1 | 9.7(8.6–10.4) | 0.33(0.31–0.36) | $1.07(0.88–1.13) \times 10^{-2}$ | 1295.0/1207 |
| | 2 | >32.5 | $= Z_1$ | $3.73(3.01–5.39) \times 10^{-3}$ | |
| 4.0–5.5 keV | 1 | 9.8(3.6–11.6) | 0.35(0.28–0.52) | $9.2(2.9–14.1) \times 10^{-3}$ | 185.2/159 |
| | 2 | 34.4(>22.2) | $= Z_1$ | $4.67(0.26 - 1.07) \times 10^{-3}$ | |

modeling of the hotter component, including a joint analysis of the *Suzaku* HXD data and the spatially-resolved *Chandra* data, is given in Sect. 5.

## 4. HXD/PIN analysis: 12–60 keV

For the PIN diodes of HXD for the energy band of 12–60 keV, the background is composed of the following three components: (i) the non-X-ray background (NXB); (ii) cosmic X-ray background (CXB); and (iii) bright point-like sources within the detector field-of-view. Of these, the NXB dominates the observed flux, particularly for faint, hard, X-ray sources, such as clusters of galaxies.

Since the NXB has a significant time-variability, the reproducibility of the NXB is the most important factor in the measurements of the hard X-ray flux from clusters of galaxies. In Sect. 4.1, the systematic error due to NXB is carefully examined. In Sect. 4.2, the CXB model is calculated. In Sect. 4.3, the point source fluxes are estimated from the *XMM-Newton* observations of the same field.

### 4.1. Non-X-ray background

The latest report from the instrument team[4] indicates that the reproducibility of the PIN NXB model for data processed by the version 2 pipeline was typically 3% ($1\sigma$). This estimate is based upon systematic comparisons between the NXB model and the PIN data during the Earth occultation in a trend archive. We check below the validity of assigning the 3% systematic error to our PIN analysis.

In Fig. 5, we show comparisons between the observed PIN data (hereafter "Data") and the NXB model in two observing periods, (a) Seq: 801013010; and (b) Seq: 801013020. In Table 5 we summarize the count rates in the 12–40 keV and 40–60 keV bands. The excess signal was detected in Data−NXB at energies below 30 keV during both observing periods. The difference in Data−NXB between two observing periods was well below the NXB itself: $(\mathrm{Data} - \mathrm{NXB})_2 - (\mathrm{Data} - \mathrm{NXB})_1 \sim 0.02(\mathrm{NXB}_1 + \mathrm{NXB}_2)/2$. However, the difference was marginally ($\sim 2\sigma$) inconsistent with zero compared with its statistical error, $(\mathrm{Data} - \mathrm{NXB})_2 - (\mathrm{Data} - \mathrm{NXB})_1 = 0.0088 \pm 0.0043$, which could indicate some residual time variability.

In general, variations in the NXB intensity depend primarily on the satellite's passage of the SAA and the COR (Kokubun et al. 2007). To study these effects, we binned the PIN spectra under the following different conditions: elapsed time after the passage of the SAA, TSAA > 6000 s, and TSAA < 6000 s, and three different COR [GV] ranges of 6 < COR < 10, 10 < COR < 12, and 12 < COR < 14. This analysis indicated that there was a trend to obtain a higher count rate for TSAA<6000 s compared with TSAA>6000 s, and a higher count rate for a smaller COR. However, the differences in the count rates were below 3% of the NXB intensity in each case.

To study the reproducibility of the NXB further, Data and NXB were compared during periods of Earth occultation. The Earth is known to be dark in hard X-rays and the Earth occultation data can be regarded as representing the NXB for the PIN observations. As a result, Data and NXB during Earth occultation show good agreement, and Data−NXB is consistent with zero. From these studies, we conclude that the systematic error in the NXB model is fairly small ($\lesssim 1\%$).

In summary, the accuracy of the PIN NXB model is consistent with that found in the latest report from the instrument team. Therefore, we adopt the instrument team's estimate of the systematic error, 3%, and propagate this through our spectral analysis of the HXD/PIN data.

[4] JX-ISAS-SUZAKU-MEMO-2007-09 by Mizuno et al.

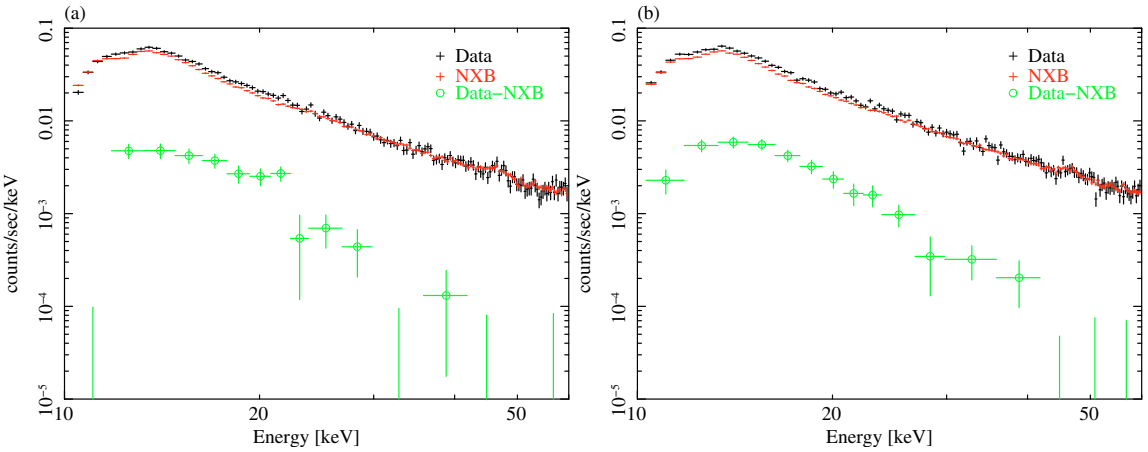


**Fig. 5.** Observed PIN spectra during two observing periods of RX J1347.5–1145. **a)** Seq: 801013010; and **b)** Seq: 801013020.In *each panel* Data, NXB, and (Data−NXB) are shown with the black crosses, red crosses, and green circles, respectively.

**Table 5.** PIN count rates measured in the 12–40 keV and 40–60 keV bands. The quoted errors are $1\sigma$ statistical errors.

| Seq | Energy range | Exposure [s] | Data $[c\,s^{-1}]$ | NXB $[c\,s^{-1}]$ | (Data–NXB) $[c\,s^{-1}]$ | (Data–NXB)/NXB % |
|---|---|---|---|---|---|---|
| 801013010 | 12–40 keV | 56 698 | 0.5180 ± 0.0030 | 0.4754 ± 0.0009 | 0.0426 ± 0.0031 | 8.96 ± 0.67 |
| 801013020 | 12–40 keV | 64 922 | 0.5223 ± 0.0028 | 0.4709 ± 0.0008 | 0.0514 ± 0.0030 | 10.92 ± 0.63 |
| 801013010+801013020 | 12–40 keV | 121 620 | 0.5203 ± 0.0021 | 0.4730 ± 0.0006 | 0.0473 ± 0.0022 | 10.00 ± 0.46 |
| 801013010 | 40–60 keV | 56 698 | 0.0497 ± 0.0009 | 0.0499 ± 0.0003 | −0.0002 ± 0.0010 | −0.44 ± 1.96 |
| 801013020 | 40–60 keV | 64 922 | 0.0497 ± 0.0009 | 0.0495 ± 0.0003 | 0.0002 ± 0.0009 | 0.43 ± 1.85 |
| 801013010+801013020 | 40–60 keV | 121 620 | 0.0497 ± 0.0006 | 0.0497 ± 0.0002 | 0.0000 ± 0.0007 | 0.03 ± 1.35 |

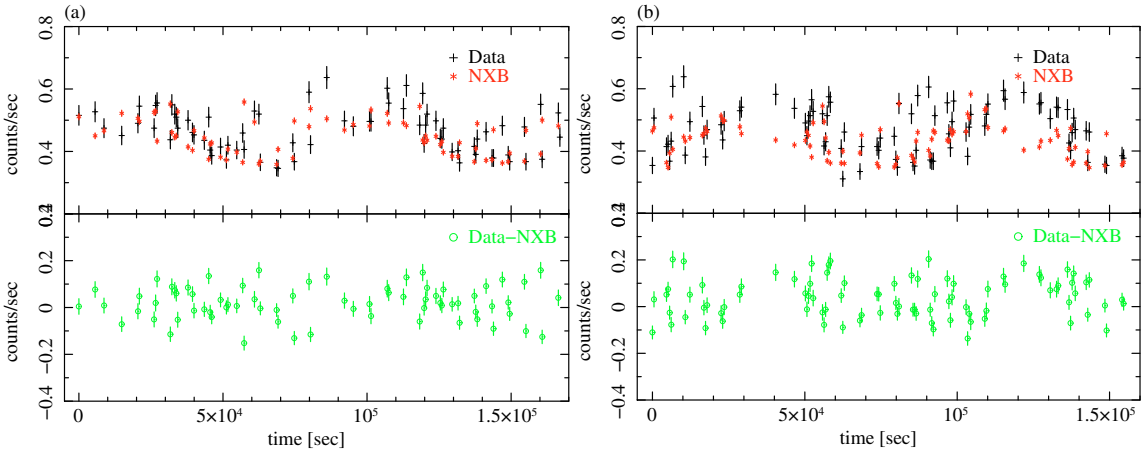


**Fig. 6.** Observed light curves of the PIN 12–40 keV count rates during two observing periods. **a)** Seq: 801013010; and **b)** Seq: 801013020. In *the upper panels*, the Data and NXB rates are shown by black and red crosses, respectively. In *the bottom panels*, (Data−NXB) is shown by the green circles. The error bars show the $1\sigma$ statistical errors.

### *4.2. Cosmic X-ray background*

We calculate the CXB spectrum in the PIN band by assuming a power-law model with an exponential cut-off at 40 keV, as previously reported from the *HEAO-1* A2 (Boldt 1987). Since the PIN detector response assumes a uniform distribution of emission over $2^\circ \times 2^\circ$ on the sky, the CXB model for a 4 square degree field in units of photons $cm^{-2}\,s^{-1}\,keV^{-1}$ is given by

$$\frac{dN}{dE} = 9.412 \times 10^{-3} \left(\frac{E}{1\ \mathrm{keV}}\right)^{-1.29} \exp\left(-\frac{E}{40\ \mathrm{keV}}\right). \quad (1)$$

The 20–50 keV energy flux of the CXB model (Eq. (1)), $5.8 \times 10^{-8}$ erg $s^{-1}$ $cm^{-2}$ $sr^{-1}$, agrees with the report of the *Beppo-SAX* observations (Frontera et al. 2007) to within about 8%. This level of uncertainty in the CXB model is smaller than the systematic error in the current NXB model. However, according to the calibration report based on the Crab observations, the PIN spectral normalization is systematically higher than the previous results given in Toor & Seward (1974) by 13%. We therefore increase CXB given in Eq. (1) by a factor of 1.13 in the simulation.

The resulting simulated CXB spectrum is shown in Fig. 7. To calculate the CXB spectrum the integration time of 100 Ms was assumed; the statistical error of the simulated spectrum is negligibly small. The CXB count rates in the 12–40 keV and 40–60 keV bands are given by $2.9 \times 10^{-2}$ and $6.1 \times 10^{-4}$ $c\,s^{-1}$, respectively, which amount to about 6.1% and 1.2% of the NXB, respectively.

Based upon the *ASCA* observations, Kushino et al. (2002) found that the CXB fluctuation in the 2–10 keV band is ∼6%, which can be attributed to the Poisson noise of the source count

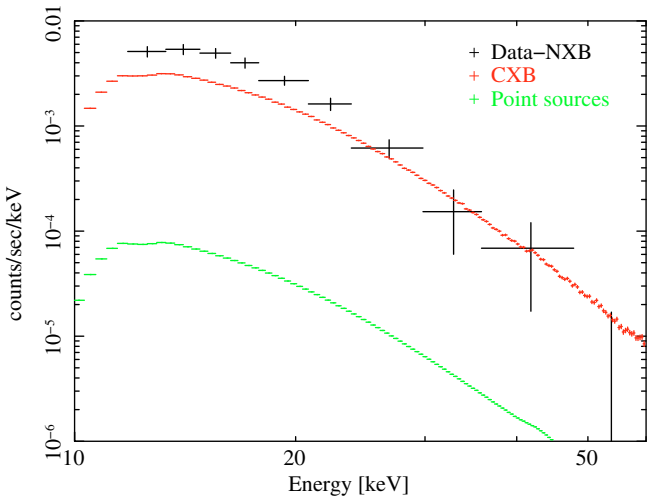


**Fig. 7.** Observed PIN spectrum minus the nominal NXB model (Data−NXB; black), the simulated CXB model (red), and the point source contribution estimated from the *XMM-Newton* observations of the same field (green).

within 0.5 degree$^2$. By scaling the *HEAO-1* result of 2.8% with the equation $\sigma_{\rm CXB} \propto \Omega^{-0.5} S^{0.25}$, where $\Omega$ and $S$ are the effective solid angle of the observation and upper cut-off flux of detectable discrete sources in the field of view, respectively (Condon 1974), Kawano et al. (2008) calculated the $1\sigma$ fluctuation of CXB to be 9.2% for the ∼100 ks HXD/PIN observations. The CXB fluctuation over the 30′ scale was therefore small compared with the NXB systematic error.

### 4.3. Hard X-ray point sources

We next estimated the hard X-ray flux of point sources inside the field-of-view of HXD/PIN from the 30 ks *XMM-Newton*/PN data of the same field (Observation ID: 0112960101). The data reduction was completed in the standard manner with `SAS` version 7.1.0, and the periods of background flares were removed with the threshold value of 0.22 c s$^{-1}$ in the 12–14 keV band.

With the `edetect_chain` program, thirty point sources were detected in the PN image. The photon index for each source was estimated from the hardness ratio, which was defined to be the ratio of the source count rates in the 0.5–1.5 keV and 1.5–5 keV band. The background was subtracted using the blank-sky data (Carter & Read 2007). The Galactic absorption was assumed in the calculation. The photon index of $\Gamma \gtrsim 2$ was obtained for almost all sources that have significant emission in the hard band. We then simulated the PIN spectrum expected for each source using a power-law spectrum with $\Gamma = 2$, where we include the PIN angular response function using `hxdarfgen`.

Figure 7 shows the spectrum of the sum of the detected sources. We found that the contribution from the point sources was totally negligible.

### 4.4. PIN source spectrum

In Fig. 8, the observed PIN spectrum with NXB and CXB subtracted is shown. In the 12–40 keV band, we detected the hard X-ray emission at the $9\sigma$ confidence level. Taking into account the NXB systematic error, however, the significance of the detection becomes far lower: the estimated count rate is $0.0187 \pm 0.0021\ (\pm 0.0142)$ c s$^{-1}$ in the 12–40 keV, where the first

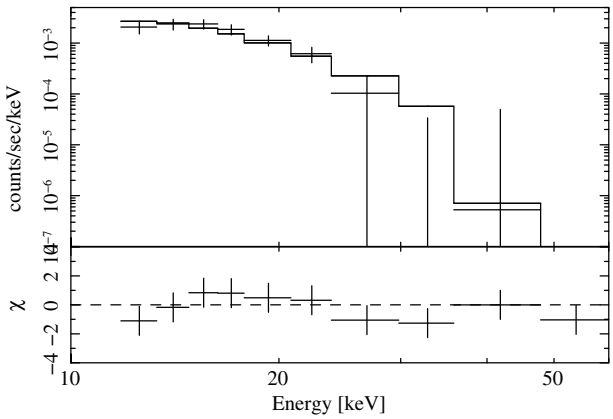


**Fig. 8.** Observed PIN spectrum with the background model subtracted (Data−NXB−CXB; the crosses) in the 12–60 keV band. The error bars indicate only the statistical errors. The histogram shows the best-fit APEC thermal plasma model. *The bottom panel* shows the residuals in units of the number of standard deviations.

and second errors are the $1\sigma$ statistical and $1\sigma$ systematic uncertainties, respectively. At higher energies, 40–60 keV, the count rate is $7 \pm 6\ (\pm 15) \times 10^{-4}$ c s$^{-1}$ ($1\sigma$); we therefore do not expect significant hard X-ray emission in the 40–60 keV band.

We next fit the single-temperature APEC model to the background-subtracted PIN spectrum in the 12–60 keV band. The XIS data is not used here. A joint analysis of XIS and HXD/PIN is presented in Sect. 5. The metal abundance was fixed at the best-fit value obtained from the XIS analysis, 0.33 solar. The systematic error in the spectral parameters due to the systematic uncertainty in the NXB model was estimated by changing the normalization factor of the NXB model by +3% or −3% and repeating the fitting procedure.

The results are shown in Fig. 8 and Table 6. We found that the temperature and normalization of the single-temperature APEC model were $kT = 20.2^{+21.4}_{-8.0}\ (^{+7.7}_{-8.7})$ keV and $1.02^{+0.95}_{-0.43}\ (^{+0.26}_{-0.26}) \times 10^{-2}$, respectively. These parameters are consistent with those obtained from the XIS data. Therefore, we conclude that the hard X-ray emission observed with PIN does indeed originate in RX J1347.5–1145.

From the observed PIN count rate and the best-fit single-temperature APEC model given in Table 2, we estimate the energy flux to be $3.8 \pm 0.5\ (\pm 3.3) \times 10^{-12}$ erg s$^{-1}$cm$^{-2}$ in the 12–60 keV ($1\sigma$). On the other hand, the previous *Beppo-SAX* observation of RX J1347.5–1145 reported detection of the hard X-ray emission at the $\sim 1.5\sigma$ significance level: $(4.0 \pm 2.6) \times 10^{-2}$ c s$^{-1}$ in the 13–60 keV band (Ettori et al. 2001), and $(6.8 \pm 4.4) \times 10^{-2}$ c s$^{-1}$ in the 20–80 keV band (Nevalainen et al. 2004). With the 12.9 keV Raymond-Smith model and the response of the PDS instrument onboard *Beppo-SAX*, the `pimms` program measures the 12–60 keV flux to be $(4.5 \pm 2.9) \times 10^{-12}$ erg s cm$^{-1}$. (All errors quoted here are $1\sigma$.) The PIN result therefore agrees with that of the PDS to within their $1\sigma$ margins of error.

## 5. XIS+HXD joint analysis

In Sect. 3, the *Suzaku* XIS data indicated the presence of a significant amount of very hot gas. In this section, we study the physical properties of this hot component, such as the amount, temperature, and metal abundance, by performing a joint analysis of the *Suzaku* data and the spatially-resolved *Chandra* spectra.

In Sect. 5.1, the properties of the ambient gas are derived from the *Chandra* data. In Sect. 5.2, the properties of the hot

**Table 6.** Single-temperature APEC model parameters fit to the PIN data in the 12–60 keV band. The systematic error in the NXB model is included in the error estimate.

| Sensor | $kT$ [keV] | $Z$ [solar] | $K$ | $\chi^2$/d.o.f. | NXB[a] |
|---|---|---|---|---|---|
| PIN | 20.2 (12.2 – 41.6) | 0.33(Fix) | $1.02(0.59–1.97) \times 10^{-2}$ | 6.7/8 | 1.00 |
| PIN | 11.5 | 0.33(Fix) | $0.76 \times 10^{-2}$ | 26.2/8 | 1.03 |
| PIN | 27.9 | 0.33(Fix) | $1.28 \times 10^{-2}$ | 6.9/8 | 0.97 |

[a] The NXB normalization factor.

gas component in the SE quadrant are derived from the *Suzaku* broad-band spectra combined with the *Chandra* data by means of a multi-temperature model. In Sect. 5.3, we argue that the hot component is described more accurately by thermal gas rather than non-thermal gas, and derive an upper limit to the possible non-thermal emission.

### 5.1. Modeling the cluster average component with *Chandra*

The deep *Chandra* ACIS-I data of RX J1347.5–1145 (Obs ID:3592, Date:2003-09-03) was analyzed with `CIAO` version 3.4 and `CALDB` version 3.3.0. After removing the periods of high background rates, the net exposure time was 56.1 ks. The backgrounds were estimated from the same detector regions of the blank-sky data, whose normalization factors were determined with the ratios of the 10–12 keV count rates.

Figure 9 shows the *Chandra* image and the azimuthally-averaged surface brightness profiles for three different position angles (0°–360°, NW: −90°–180°, and SE: 180°–270°). The cluster emission extends out to $r = 5' \sim 1.7$ Mpc, and significant excess emission is visible in $10'' \lesssim r \lesssim 60''$ for the SE quadrant.

To derive the average temperature profile within 5′, we extracted the spectra for the following six radial bins in the NW region, i.e. the region outside of the SE quadrant: 0–4″, 4″–8″, 8″–24″, 24″–56″, 56″–120″, and 120″–300″. The radial bins were chosen such that the temperature profile was measured with sufficient spatial resolution and a statistical accuracy of ∼20%.

Figure 10 shows the projected temperature profile, i.e. the temperature profile determined from the simple APEC model fit to each radial bin in the NW region. Our estimate of the projected temperature profile derived from the *Chandra* ACIS-I data agrees with the previous *Chandra* ACIS-S results reported by Allen et al. (2002) to within the statistical errors, particularly in the central 100″ region. Based on the ACIS-I spectral simulations, we also confirmed, assuming the same photon statistics as the present observation, that we could securely determine the temperature of each bin including the high-temperature (∼18 keV) regions between 24″ and 120″.

Since each spectrum is a superposition of the cluster emission from any point along the line of sight, we correct for this effect, or "deproject" our observations, by using the PROJCT model in the `XSPEC` software and fitting the six radial bins simultaneously with the assumption that the temperature distribution is spherically symmetric. As noted by Allen et al. (2002), the metal abundance gradient is marginally detected in the *Chandra* data; however, the large uncertainty in the metal abundance measurement does not warrant its treatment as a free function. We therefore assume that the metal abundance distribution is uniform and ignore the abundance gradient.

The resulting deprojected temperature profile in the NW region is shown in Fig. 10 and the best-fit parameters are given in Table 7. Henceforth, we refer to the best-fit model presented in Table 7 as the "6APEC model."

### 5.2. Temperature measurement of the SE clump

The 6APEC model in Sect. 5.1 described the average temperature structure of ambient gas, measured from the NW region. We subtracted the flux inferred by this model from the *Suzaku* data, and studied the nature of the excess emission in the SE quadrant.

We added another APEC model to describe the hot component in the SE quadrant. We used the best-fit parameters for $kT$ and $K$ given in Table 7 for the ambient gas (6APEC model), and used the *Suzaku* data, both the XIS and PIN spectra, to constrain the temperature, $kT_{\rm ex}$, and the normalization, $K_{\rm ex}$, of the excess component in the SE quadrant. As for the metal abundance, the abundance was assumed to be equal to all of the six radial bins of ambient gas, as well as to the excess component, i.e. a single abundance was applied to the entire cluster. We did this because the metal abundance was not constrained well by the *Chandra* data.

We found that the *Chandra* data tended to infer systematically higher values for $kT$ and $K$ than the XIS data did. To correct for the difference between their instrumental calibrations, we multiplied the 6APEC model by the PLABS model, $M(E) = E^{-\alpha}$, with $\alpha = 0.02$ ($E$ is the energy of photons), and used the relative normalization factor of 0.93. In Appendix A, we provide more details on the *Suzaku*-*Chandra* cross-calibration.

Figure 11 and Table 8 show the results of the 6APEC×PLABS + APEC model fit to the XIS (0.5–10 keV) and PIN (12–60 keV) data. To show the degree of systematic errors due to the uncertainty in the *Suzaku*-*Chandra* cross-calibration, we also show the parameters for $\alpha = 0$ and 0.03 in Table 8. From these results, we conclude that the temperature of the excess emission in the SE quadrant is $kT_{\rm ex} = 25.3^{+6.1}_{-4.5}\,(^{+6.9}_{-9.5})$ keV, where the first error is statistical and the latter is systematic (both 90% confidence levels). In Table 8, we also show the fitted parameters when only XIS was used. Due to the high photon statistics of XIS, the temperature of the SE excess component can be constrained to be $kT^{\rm XIS}_{\rm ex} = 24.8^{+6.1}_{-4.6}\,(^{+6.8}_{-9.5})$ keV. However, the spectral cut-off at $25/(1+z) \sim 17$ keV coincides with the PIN band, which suggests the importance of the broad-band spectroscopy in the present study. As for the other quantities, we found from the XIS+PIN joint analysis that the metal abundance was 0.38(0.35–0.41) solar, and the absorption-corrected X-ray luminosity of the excess component was $L_{\rm X,ex} = 1.4 \times 10^{45}$ erg s$^{-1}$ in the 0.5–10 keV, and $1.2 \times 10^{45}$ erg s$^{-1}$ in the 12–60 keV.

Since the determination of $kT_{\rm ex}$ from X-ray spectroscopy is the central result of this paper, we estimate the other potential source of systematic errors in our analysis. Specifically, we examine: (i) the assumption of constant metal abundance for all radii; (ii) the suitability in the choice of the SE region; and (iii) effects of the uncertainty in the 6APEC model parameters. (i) What if the metal abundance of the ambient gas differs from that of the excess component? What if an abundance gradient exists in the ambient gas? To explore these possibilities, we considered the metal abundance of the excess component, $Z_{\rm ex}$, as well as

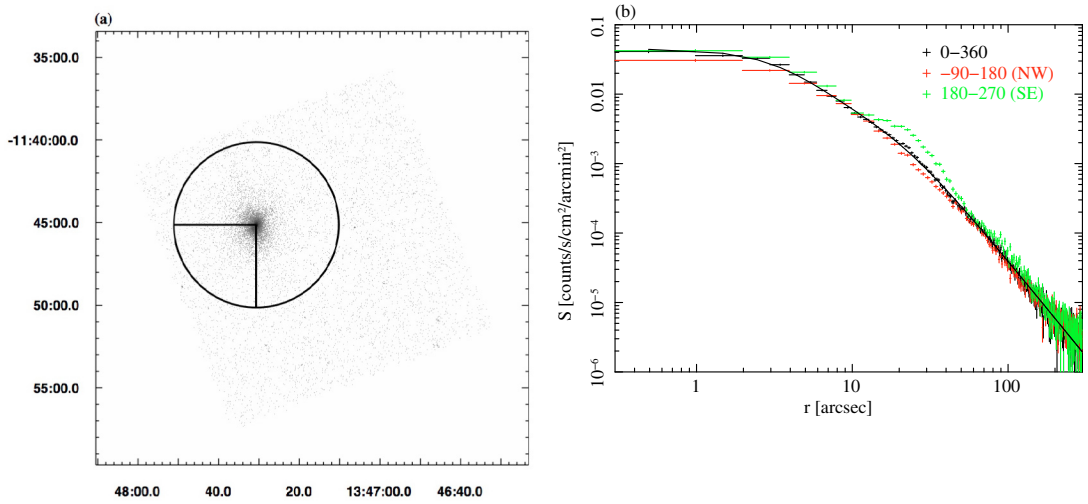


**Fig. 9. a)** *Chandra* ACIS-I image in the 0.5–7 keV band. The solid lines show the NW and SE regions. The radius of the circle is 5′. **b)** The surface brightness profiles of the position angle 0°–360° (black), NW: −90°–180° (red), and SE:180°–270° (green). The black line shows the best-fit double $\beta$-model for the position angle of 0°–360°.

that of the ambient gas in two larger radial bins, $0'' < r < 8''$ and $8'' < r < 300''$, as free parameters, and fitted them simultaneously. We found that $kT_{\rm ex} = 26.3$ keV, $Z_{\rm ex} < 1.8$ solar, and $K_{\rm ex} = 2.16 \times 10^{-3}$ ($\chi^2$/d.o.f. = 1306/1217), which are consistent with the values given in Table 8. As for the metal abundance of the ambient gas, we found that $Z \sim 0.64$ solar and 0.22 solar in $0'' < r < 8''$ and $8'' < r < 300''$, respectively; (ii) from the *Chandra* image, we can observe that the excess emission appears to extend over slightly more than the SE quadrant. How does this affect the determination of $kT_{\rm ex}$? We repeated our analysis with the SE and NW regions redefined as (180°–315°) and (−45°–180°), respectively. We measured $kT_{\rm ex} = 20.0$ keV, $K_{\rm ex} = 2.87\times10^{-3}$, and $Z_{\rm ex} = Z = 0.37$ solar with $\chi^2$/d.o.f. = 1315/1219. Therefore, selecting the SE region did not affect the best-fit parameters significantly; (iii) the statistical errors in the 6APEC model parameters had not been propagated through the spectral fitting of the SE quadrant, except for the cross-calibration error in the spectral slope, which was included by varying $\alpha$ from 0 to 0.03. To address this, we completed simultaneous APEC fits to the *Chandra* spectra in 6 radial bins (without deprojection) as well as to the *Suzaku* XIS and PIN spectra, for which we used the 6 APEC models multiplied by the $\alpha = 0.02$ PLABS model, and then added to the additional APEC model. We found that $kT_{\rm ex} > 26$ keV, $Z_{\rm ex} = 0.38(0.35–0.41)$ solar, and $K_{\rm ex} = 2.16(1.96–2.41)\times10^{-3}$ ($\chi^2$/d.o.f. = 1676/1510). Although the temperature was not well constrained in this case, it was of a high value. From these studies we conclude that our estimate, $kT_{\rm ex} = 25.3^{+6.1}_{-4.5}$ ($^{+6.9}_{-9.5}$) keV, is robust.

Finally, as a consistency check, we analyzed the *Chandra* spectrum of the SE quadrant ($r < 5'$) on its own, without the *Suzaku* data, in the same manner. The best-fit parameters for the excess component were $kT_{\rm ex}^{\rm Chandra} = 31.1^{+24.1}_{-12.6}$ keV, $Z_{\rm ex}^{\rm Chandra} = 0.49^{+0.15}_{-0.15}$ solar, and $K_{\rm ex}^{\rm Chandra} = 1.47^{+0.21}_{-0.15} \times 10^{-3}$ ($\chi^2$/d.o.f. = 320/332). Therefore, both the *Chandra*-alone analysis and the joint Chandra+*Suzaku* analysis implied that the excess emission had a temperature in excess of 20 keV[5].

[5] As for the normalization factor, $K_{\rm ex}^{\rm Chandra}$ was found to be smaller than that from the joint analysis by about 35%. This can be explained by the difference in their integration regions. On the other hand, this level of difference amounts to only a few% of the total cluster emission, and is comparable to the calibration errors of the instruments. Therefore, we simply assigned 30% systematic error to $K_{\rm ex}$.

Compared with the results for the *Chandra* data alone, the joint *Chandra*+*Suzaku* broad-band data analysis yielded a far more accurate determination of $kT_{\rm ex}$. The *Suzaku*'s unprecedented sensitivity over the wide X-ray band made it possible to determine, for the first time, the temperature of the hot gas in the ICM solely from the X-ray spectroscopy without the help of SZ effect data.

### 5.3. Constraint on the non-thermal emission

We had been assuming that the excess hard X-ray emission from the SE quadrant is thermal; could it, however, be non-thermal? If so, our derived temperature must be reconsidered.

To address this question, the XIS and PIN data were re-analyzed in light of non-thermal emission. While the 6APEC thermal plasma model was again used for the ambient gas, the APEC model was replaced with a power-law (PL) spectrum for describing the excess component. We then fitted the new model, "6APEC× PLABS+PL model", to the observed XIS and PIN data. The amplitude (normalization), a power-law index, $\Gamma$, of the non-thermal component, and the metal abundance of the ambient gas were treated as free parameters.

Figure 12 shows the results, and Table 9 lists the best-fit parameters. We found that the power-law index is given by $\Gamma \sim 1.5$, or more precisely $\Gamma = 1.45^{+0.03}_{-0.04}$ ($^{+0.09}_{-0.04}$). The reduced $\chi^2$ of this model, $\chi^2 = 1317.1/1219$ (see Table 9), was slightly higher than that for the thermal model, $\chi^2 = 1315.1/1219$ (see Table 8), and negative residuals were seen in consecutive bins above 22 keV.

We examined the non-thermal model more closely. In the XIS band below 10 keV, the non-thermal model with $\Gamma = 1.5$ and the thermal APEC model with 25 keV could hardly be distinguished. However, the observed PIN spectrum was far *softer* than $\Gamma = 1.5$, the effective photon index being $\Gamma_{\rm eff} \sim 3$. When we fitted the 6APEC× PLABS+PL model to the PIN data alone, the 90% lower bound on the photon index was found to be $\Gamma > 1.8$[6], which was significantly above the 90% upper bound on $\Gamma$ from the XIS data, $\Gamma < 1.5$. We further checked that fixing the power-law index to $\Gamma = 2.0$, as predicted from the non-thermal bremsstrahlung in the strong shock limit (Sarazin & Kempner 2000), yielded a poor fit to the XIS and PIN data; the

[6] The systematic errors due to both the NXB model and the *Suzaku*-*Chandra* cross-calibration are included.

reduced $\chi^2$ was 1708 for 1220 degrees of freedom. Therefore, it appears difficult to explain the SE excess component with the non-thermal PL model.

Given that the excess component was described more accurately by thermal emission than non-thermal emission, we derived an upper limit to the non-thermal emission to characterize the SE component. We fixed the metal abundance and the PL index to be 0.38 solar and $\Gamma = 1.5$, respectively. The 6APEC model, modified by the $\alpha = 0.02$ PLABS model, was again used for describing the ambient gas.

The derived upper limits are given in Table 10. Taking into account the NXB systematic error of the PIN detector, the $3\sigma$ upper limit to the non-thermal flux in the 12–60 keV, $F_{\rm HXR}$, was estimated to be $F_{\rm HXR} < 2.1 \times 10^{-11}$ erg s$^{-1}$ cm$^{-2}$ from the PIN analysis, and $F_{\rm HXR} < 8 \times 10^{-12}$ erg s$^{-1}$ cm$^{-2}$ from the XIS+PIN simultaneous fit. Here, the $1\sigma$ error was calculated by adding the $1\sigma$ statistical error and the $1\sigma$ systematic error in quadrature.

## 6. Discussion

Using the deep broad-band observations of RX J1347.5–1145 with *Suzaku*, the temperature structure has been determined with particular attention to the extremely hot gas. We have found that a multi-temperature thermal emission model including a very hot ($kT_{\rm ex} \sim 25$ keV) component fits the wide-band spectra well. We have also placed an upper limit on the non-thermal hard X-ray emission.

In Sect. 6.1, our results are compared with previous X-ray and radio observations, and examine further the physical properties of the SE clump. In Sect. 6.2, our results are compared with those for the radio mini halo in this cluster discovered from 1.4 GHz radio observations to estimate the magnetic-field strength in the ICM.

### 6.1. Properties of the extremely hot gas

From the analysis of the *Suzaku* spectra of RX J1347.5–1145, the temperature of the SE excess emission was obtained to be $kT_{\rm ex} = 25.3^{+6.1}_{-4.5}\,(^{+6.9}_{-9.5})$ keV (90% confidence level; the first error being statistical and the second, systematic). This was in an excellent agreement with the previous measurement by Kitayama et al. (2004), $28.5 \pm 7.3$ keV (68%; statistical only), from a joint analysis of the SZ data (Komatsu et al. 1999, 2001) and the *Chandra* ACIS-S3 data (Allen et al. 2002). Here, we compare our X-ray-only results with their SZ+X-ray results.

We estimate the gas density and gas mass of the SE excess component from the *Suzaku* and *Chandra* data. For simplicity, we assume that the extremely hot gas is uniformly distributed within a sphere of a radius $R = 25'' \sim 144$ kpc (because the excess is present in $10'' < r < 60''$; Fig. 9b). Using the measured spectral normalization, $K_{\rm ex}$, which depends on $n_{\rm e} n_{\rm H} V$ (where $V = 4\pi R^3/3$ is the volume of the gas and $n_{\rm H} = 0.86 n_{\rm e}$), the electron density, $n_{\rm e,ex}$, and the gas mass, $M_{\rm gas,ex}$, are obtained as:

$$n_{\rm e,ex} = (1.6 \pm 0.2) \times 10^{-2} \left( \frac{V_{\rm ex}}{3.6 \times 10^{71}\ {\rm cm}^3} \right)^{-1/2} {\rm cm}^{-3}, \quad (2)$$

$$M_{\rm gas,ex} = (5.6 \pm 0.8) \times 10^{12} \left( \frac{V_{\rm ex}}{3.6 \times 10^{71}\ {\rm cm}^3} \right)^{1/2} M_\odot. \quad (3)$$

Here, we have propagated the systematic error in $K_{\rm ex}$ through to the final results (Sect. 5.2). These results may be compared with those obtained in Kitayama et al. (2004): $n_{\rm ex} = (1.49 \pm 0.59) \times 10^{-2}$ cm$^{-3}$ and $M_{\rm gas,ex} \sim 2 \times 10^{12}\ M_\odot$. While the inferred number densities are in an excellent agreement, the gas mass from our analysis is more than a factor of two higher than that from Kitayama et al. (2004); however, the uncertainty in the gas mass estimate from Kitayama et al. (2004) is high enough for them to be consistent. (The uncertainty is large because they did not assume spherical geometry for the excess component, and the line-of-sight extension of the SE component was poorly constrained.)

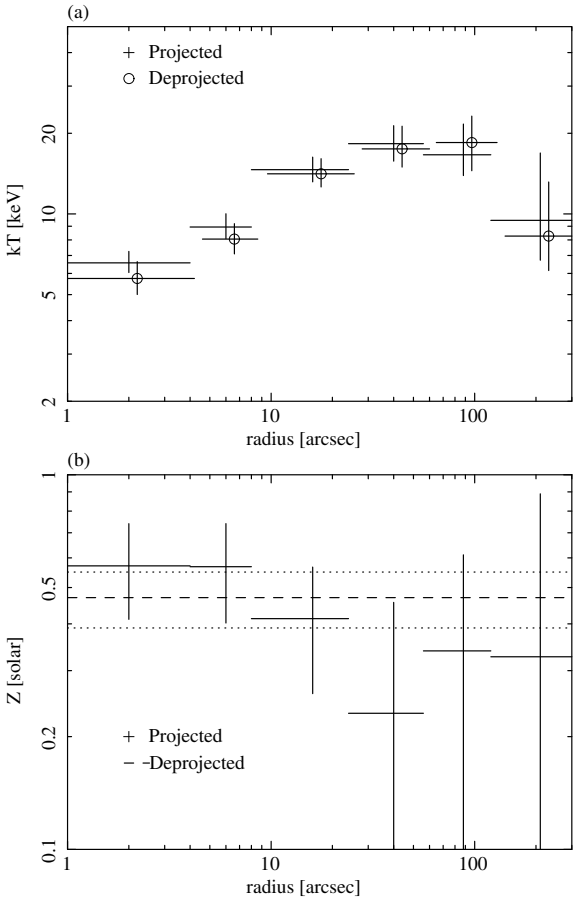


**Fig. 10. a)** Projected (crosses) and deprojected (circles) temperature profiles measured from the *Chandra* data in the NW region. **b)** Projected metal abundance profile (crosses). The horizontal dashed and dotted lines show the best-fit constant abundance and the corresponding 90% confidence interval obtained from the deprojection analysis, respectively. We assume that the metal abundance is constant over all radial bins throughout this paper.

How does the excess component compare with the remainder of the cluster? The average (ambient) temperature and gas density for $10'' < r < 60''$, excluding the SE quadrant, are $kT \sim 15$ keV from the *Chandra* spectrum and $n_{\rm e} \sim 6.6 \times 10^{-3}$ cm$^{-3}$ from Eqs. (3)–(5) of Kitayama et al. (2004), respectively. Thus, the SE clump exhibits the temperature and the density that are higher than the ambient gas in the same radial bins by factors of 1.7 and 2.4, respectively. This means that the excess hot component is over-pressured, and such a region is expected to be short-lived, ~0.5 Gyr (Takizawa 1999).

As already discussed in Kitayama et al. (2004), the gas properties can be explained by a fairly recent (within the last 0.5 Gyr or so), bullet-like high velocity ($\Delta v \sim 4500$ km s$^{-1}$) collision of two massive ($5 \times 10^{14}\ M_\odot$) clusters.

The heat energy of the SE clump is also estimated to be $E_{\rm th,ex} = (3/2) kT_{\rm ex} (n_{\rm e,ex} + n_{\rm H,ex}) V_{\rm ex} \sim 6 \times 10^{62}$ erg. This enormous amount of energy cannot be easily produced by a central

**Table 7.** Parameters of the "6APEC model", including estimates of the deprojected temperature profile from the *Chandra* ACIS-I data at the six annular bins in the NW region, which excludes the SE quadrant.

| Radius [″] | $kT$ [keV] | $Z$ [solar][a] | $K^b$ | $\chi^2$/d.o.f. |
|---|---|---|---|---|
| 0–4 | 5.74 (5.01–6.64) | 0.47 (0.39–0.55) | $0.97\ (0.92–1.02) \times 10^{-3}$ | 364.2/290 |
| 4–8 | 8.06 (7.10–9.20) | | $1.83(1.77–1.89)\ \times 10^{-3}$ | |
| 8–24 | 14.12 (12.61–16.08) | | $4.02(3.93–4.10) \times 10^{-3}$ | |
| 24–56 | 17.49 (14.95–21.26) | | $2.86(2.79–2.95) \times 10^{-3}$ | |
| 56–120 | 18.47 (14.49–23.18) | | $2.29(2.22–2.37) \times 10^{-3}$ | |
| 120–300 | 8.27 (6.15–13.16) | | $0.91(0.86 - 0.97) \times 10^{-3}$ | |

[a] The metal abundance is assumed to be common for all radial bins; [b] $K$ represents the normalization factor for each spherical shell, i.e., the position angle of 0°–360°, of the fitting.

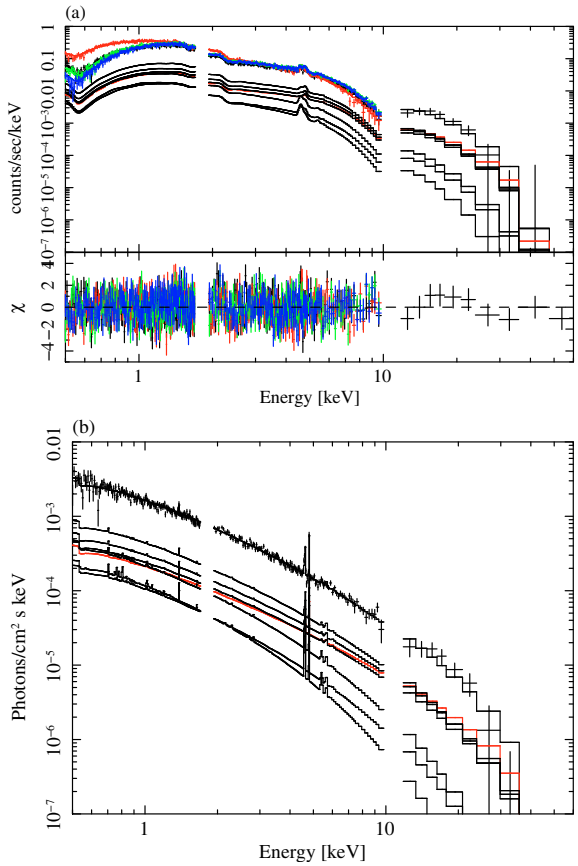


**Fig. 11. a)** 6APEC×PLABS($\alpha$ = 0.02) + APEC model, fit simultaneously to the observed XIS (0.5–10 keV) and PIN (12–60 keV) spectra. The spectra taken by four sensors, XIS-0 (black), 1 (red), 2 (green), and 3 (blue), are shown separately. The black and red lines show the ambient component (6APEC × PLABS) and the excess hot component described by an additional APEC model, respectively, convolved with the telescope and the detector response functions. In *the bottom panel* the residuals of the fit in units of the number of standard deviations are shown. We have used the nominal NXB model for the background of the PIN data (see Sect. 4.1). **b)** same as **a)**, but for the unfolded XIS-0 and PIN spectra.

source in the cluster: one would need an AGN with $10^{46}$ erg s$^{-1}$ for at least 1 Gyr and to place the energy into the SE region without any radiative loss. On the other hand, cluster mergers, which are the most energetic events in the Universe after the Big Bang, will most naturally explain this high energy phenomenon. Therefore, our results support a merger scenario, on the basis of the X-ray spectroscopic data alone without the help of SZ data.

### 6.2. Estimation of the magnetic field

On the basis of our upper limit to the non-thermal hard X-ray emission derived from *Suzaku* HXD/PIN data, what can be learned about the underlying physics of the cluster X-ray emission? The non-thermal hard X-ray emission is produced by the inverse Compton (IC) scattering of relativistic electrons off the Cosmic Microwave Background (CMB) photons, and the same population of electrons also generate synchrotron radiation. From the exact derivations by Blumenthal & Gould (1970), equations for the synchrotron emission at the frequency $\nu_{\rm Syn}$ and the IC emission at $\nu_{\rm IC}$ are:

$$\frac{{\rm d}W_{\rm Syn}}{{\rm d}\nu_{\rm Syn}{\rm d}t} = \frac{4\pi N_0 {\rm e}^3 B^{(p+1)/2}}{m_{\rm e}c^2}\left(\frac{3{\rm e}}{4\pi m_{\rm e}c}\right)^{-(p-1)/2} a(p)\nu_{\rm Syn}^{-(p-1)/2}, \quad (4)$$

$$\frac{{\rm d}W_{\rm IC}}{{\rm d}\nu_{\rm IC}{\rm d}t} = \frac{8\pi^2 r_0^2}{c^2} h^{-(p+3)/2} N_0 (k_B T_{\rm CMB})^{(p+5)/2} F(p) \nu_{\rm IC}^{-(p-1)/2}, \quad (5)$$

where $N_0$ and $p$ are the normalization and the power-law index of the electron distribution, $N(\gamma) = N_0\gamma^{-p}$ ($\gamma$ is the Lorentz factor of the electron), $h$ is the Planck constant, $T_{\rm CMB}$ is the CMB temperature, and $T_{\rm CMB} = 2.73(1 + z)$ K. The functions $a(p)$ and $F(p)$ are defined as follows:

$$a(p) = \frac{2^{(p-1)/2}\sqrt{3}\Gamma\left(\frac{3p-1}{12}\right)\Gamma\left(\frac{3p+19}{12}\right)\Gamma\left(\frac{p+5}{4}\right)}{8\pi^{1/2}(p+1)\Gamma\left(\frac{p+7}{4}\right)}, \quad (6)$$

$$F(p) = \frac{2^{p+3}(p^2+4p+11)}{(p+3)^2(p+5)(p+1)}\Gamma\left(\frac{p+5}{2}\right)\zeta\left(\frac{p+5}{2}\right). \quad (7)$$

Equations (4) and (5) give the total emitted powers per volume per frequency in the rest frame. Given that both powers are diminished by the same dimming factor, the ratio of observed flux densities of the synchrotron and IC emission, $S_{\rm Syn}/S_{\rm IC}$, is equal to $({\rm d}W_{\rm Syn}/{\rm d}\nu_{\rm Syn}{\rm d}t)/({\rm d}W_{\rm IC}/{\rm d}\nu_{\rm IC}{\rm d}t)$, and the strength of the magnetic field $B$ can be directly estimated.

We find $S_{\rm IC} < 0.11$ $\mu$Jy from our limit on the non-thermal hard X-ray emission for electrons with the IC emission energy (frequency) of 12 keV ($\nu_{\rm IC} = 2.9 \times 10^{18}(1 + z)^{-1}$ Hz). As for $S_{\rm Syn}$, Gitti et al. (2007a) discovered extended (~500 kpc) radio emission in RX J1347.5–1145 based on their low (18″) resolution VLA observations and higher (2″) resolution data in the VLA archive. They subtracted the contribution of discrete radio sources and estimated the total flux density of the diffuse radio emission to be $S_{\rm Syn} = 25$ mJy at $\nu_{\rm Syn} = 1.4(1 + z)^{-1}$ GHz. Combining these numbers with Eqs. (4) and (5), a lower bound to the magnetic-field strength in the ICM is obtained such that $B > 0.007$ $\mu$G for $p = 2\Gamma - 1 = 2$. The estimation is sensitive to the assumption of $p$: for example, in the case of $p = 3$, $B > 0.072$ $\mu$G.

**Table 8.** Spectral parameters for the SE excess component obtained from the 6APEC × PLABS + APEC model fit to the XIS+PIN data and the XIS data.

| | APEC | | | | |
|---|---|---|---|---|---|
| Sensor | $kT_{ex}$ [keV] | $Z_{ex}$ [solar][a] | $K_{ex}$ | $\chi^2$/d.o.f. | $\alpha^b$ |
| XIS0–3+PIN | 25.3(20.8–31.4) | 0.38(0.35–0.41) | $2.14(2.05–2.24) \times 10^{-3}$ | 1311.1/1219 | 0.02 |
| XIS0–3+PIN | 15.8 | 0.36 | $1.98 \times 10^{-3}$ | 1313.1/1219 | 0.00 |
| XIS0–3+PIN | 32.2 | 0.39 | $2.26 \times 10^{-3}$ | 1310.2/1219 | 0.03 |
| XIS0–3 | 24.8(20.2–30.9) | 0.38(0.35–0.41) | $2.00(1.91–2.09) \times 10^{-3}$ | 1303.3/1209 | 0.02 |
| XIS0–3 | 15.5 | 0.36 | $1.84 \times 10^{-3}$ | 1303.7/1209 | 0.00 |
| XIS0–3 | 31.9 | 0.39 | $2.11 \times 10^{-3}$ | 1303.0/1209 | 0.03 |

[a] The metal abundance is assumed to be the same for all the APEC components, including the ambient gas as well as the excess component; [b] the power-law index of the PLABS model, coming from the *Suzaku-Chandra* cross-calibration (see text).

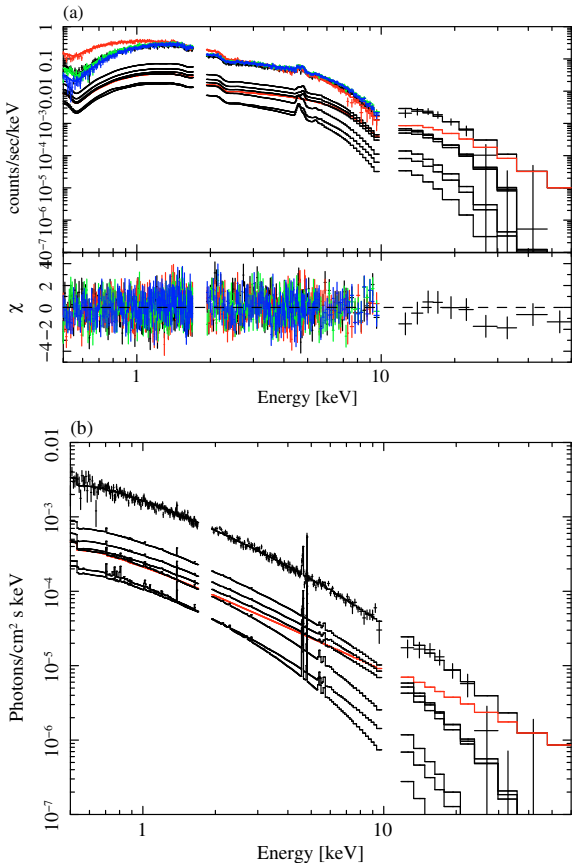


**Fig. 12. a)** 6APEC×PLABS($\alpha$ = 0.02) (thermal model for the ambient gas) + PL model (non-thermal model for the hot gas), fit simultaneously to the observed XIS (0.5–10 keV) and PIN (12–60 keV) spectra. The spectra taken by four sensors, XIS-0 (black), 1 (red), 2 (green), and 3 (blue), are shown separately. The black and red lines show the ambient component (6APEC×PLABS) and the excess hot component described by a non-thermal power-law model, respectively, convolved with the telescope and the detector response functions. In *the bottom panel* the residuals of the fit in units of the number of standard deviations are shown. We have used the nominal NXB model for the background of the PIN data (see Sect. 4.1). **b)** same as **a)**, but for the unfolded XIS-0 and PIN spectra.

This limit, though weak, is consistent with typical values found for other clusters, $B \sim 0.1$–$1$ $\mu$G, based on *RXTE* and *Beppo-SAX* observations (e.g. Rephaeli et al. 2008). Our result also agrees with results for *Suzaku* observations of a merging cluster A3376 at $z = 0.046$, $B > 0.03$ $\mu$G (Kawano et al. 2008). However, the previous measurements were derived mostly for nearby ($z < 0.1$) clusters as well as some medium-redshift clusters, such as A2163 at $z = 0.20$ (Rephaeli et al. 2006) and the Bullet cluster at $z = 0.296$ (Petrosian et al. 2006). Our work provides a constraint on the cluster magnetic-field strength at a higher redshift, $z = 0.451$.

## 7. Summary

We have reported results of an analysis of *Suzaku* wide-band (0.5–10 keV with XIS and 12–60 keV with HXD/PIN) X-ray spectroscopic observations of the most luminous X-ray cluster, RX J1347.5–1145, at $z = 0.451$, to investigate the temperature structure of the ICM, signatures of a recent violent merger, as well as signatures of the non-thermal emission.

This cluster is known to contain a very hot gas clump that produces excess emission of the ambient gas that follows more-or-less the conventional $\beta$ model (Komatsu et al. 2001; Allen et al. 2002; Kitayama et al. 2004). The temperature of this gas clump was not measured accurately from the previous X-ray spectroscopic observations, because the sensitivities degraded significantly at energies above 10 keV.

Our re-analysis of the *Chandra* data confirmed the result of previous work, and yielded a poor limit on the temperature of the excess hot component, $kT_{ex}^{Chandra} = 31.1^{+24.1}_{-12.6}$ keV (90% confidence level; statistical). When the hard X-ray data from the *Suzaku* XIS spectra in the 0.5–10 keV region and the HXD/PIN data in the 12–60 keV were combined with the *Chandra* data, we finally obtained a good measurement of the temperature, $25.3^{+6.1}_{-4.5}$ ($^{+6.9}_{-9.5}$) keV (90% confidence level; statistical and systematic), which was in excellent agreement with that derived from the previous joint analysis of the SZ effect and X-ray imaging observations (Kitayama et al. 2004). We emphasize that this is the first time that X-ray spectroscopic observations alone have enabled a robust analysis of such a high temperature gas component, due to *Suzaku*'s unprecedented sensitivity over the wide X-ray band.

We have found that the broad-band X-ray spectrum is described more accurately by a thermal plasma model instead of a non-thermal power-law model. The present result therefore confirms the presence of the hottest *thermal* gas in the cluster. The most likely explanation for this phenomena is a recent violent merger at a collision velocity of ~4500 km s$^{-1}$, similar to that inferred for the Bullet cluster (Milosavljević et al. 2007; Springel & Farrar 2007; Mastropietro & Burkert 2007; Nusser 2008).

The upper bound on the non-thermal flux in the 12–60 keV band, $F_{HXR} < 8 \times 10^{-12}$ erg s$^{-1}$ cm$^{-2}$, yields, when combined with the discovery of a radio mini halo in this cluster by Gitti et al. (2007a), a lower bound to the ICM magnetic-field

**Table 9.** Spectral parameters for the SE excess component obtained from the 6APEC × PLABS+non-thermal power-law (PL) model fit to the XIS+PIN data.

| | Power-law | | 6APEC | | |
|---|---|---|---|---|---|
| Sensor | $\Gamma$ | Normalization | $Z$ [solar] | $\chi^2$/d.o.f. | $\alpha$ |
| XIS0–3+PIN | 1.45(1.41–1.48) | $2.58(2.30–2.52) \times 10^{-4}$ | 0.42(0.39–0.45) | 1317.1/1219 | 0.02 |
| XIS0–3+PIN | 1.54 | $2.57 \times 10^{-4}$ | 0.40 | 1312.5/1219 | 0.00 |
| XIS0–3+PIN | 1.41 | $2.58 \times 10^{-4}$ | 0.42 | 1321./1219 | 0.03 |

**Table 10.** Limits on the amplitude (normalization) of a non-thermal power-law (PL) component with $\Gamma = 1.5$ as the explanation of the excess hard X-ray emission in the SE quadrant.

| Sensor | Model[a] | Normalization[b] | | $\chi^2$/d.o.f.[c] | | Flux(12–60 keV)[d] |
|---|---|---|---|---|---|---|
| | | NXB × 1.00 | NXB × 0.97 | NXB × 1.00 | NXB × 0.97 | [erg s$^{-1}$ cm$^{-2}$] |
| PIN | APEC+PL | ~0 | $5.1 \times 10^{-4}$ | 7.2/7 | 4.6/7 | $<2.11 \times 10^{-11}$ |
| XIS0–3+PIN | APEC+PL | $<1.6 \times 10^{-4}$ | $2.0 \times 10^{-4}$ | 1310.2/1218 | 1344.3/1218 | $<8.2 \times 10^{-12}$ |
| PIN | PL | $1.8(0.7–2.9) \times 10^{-4}$ | $6.3 \times 10^{-4}$ | 8.8/9 | 5.1/9 | $<2.15 \times 10^{-11}$ |
| XIS0–3+PIN | PL | $2.48(2.39–2.59) \times 10^{-4}$ | $2.52 \times 10^{-4}$ | 1322.8/1220 | 1351.9/1220 | $<3.8 \times 10^{-12}$ |

[a] The spectral model for the SE excess emission; [b] the amplitude (normalization) of the power-law component after removing the NXB models with rescaling factors of 1 and 0.97. The error and limits are the $1\sigma$ bound; [c] the values of $\chi^2$ and the number of degrees of freedom; [d] the $3\sigma$ upper limit on the energy flux of the power-law component in the 12–60 keV band.

strength, $B > 0.007$ $\mu$G for the electron index of 2. These constraints provide valuable information on the non-thermal nature of the cluster gas and the particle acceleration in a high-redshift universe. However, the accuracy of the present measurement of the hard X-ray emission is limited by the sensitivity of the instrument. If the magnetic field in RX J1347.5–1145 was comparable to that of the other clusters, $B \sim 0.1$ $\mu$G, a 50-fold higher sensitivity would be required to detect non-thermal hard X-ray emission from this cluster. We expect that future X-ray missions (e.g. *NeXT*; Takahashi et al. 2008) will determine the non-thermal X-ray flux more accurately and draw more definitive conclusions.

Before the advent of the *Suzaku* satellite, it was difficult to measure the high-temperature ($\gg$10 keV) gas in the X-ray band reliably, due to limited sensitivity. The present paper demonstrates the power of broad-band X-ray spectroscopy in the study of gas heating due to a cluster merger, which is complementary to observations of the SZ effect. In the near future, we expect the number of merging clusters observed with *Suzaku* to increase rapidly, which should shed new light on the physics of these violent mergers.

*Acknowledgements.* We are grateful to the *Suzaku* team members for the operation and the instrument calibrations. We also thank H. Böhringer, T. Ohashi, K. Masai, N. Y. Yamasaki, K. Mitsuda, and R. Smith for discussions and comments. NO acknowledges support from the Alexander von Humboldt Foundation in Germany. This work is supported in part by the Grant-in-Aid by the Ministry of Education, Culture, Sports, Science and Technology, 19740112 (NO) and 18740112 (TK). E.K. acknowledges support from an Alfred P. Sloan Research Fellowship.

## Appendix A: The *Suzaku-Chandra* cross calibration

Because the temperature measurement of very hot gas based on a spectral fit is sensitive to subtle changes in the spectral slope, a precise calibration of the effective area is critical. In the analysis of XIS+HXD spectra (Sect. 5), we have modeled the cluster average emission with *Chandra*. The cross-calibration between *Suzaku*/XIS and *Chandra*/ACIS-I data is therefore mandatory.

If the global cluster spectrum is accumulated from a $r < 5'$ circular region with the *Chandra*/ACIS-I data, the APEC model fitting infers $kT = 14.4(13.6–15.3)$ keV, $Z = 0.45(0.38–0.52)$ solar, $K = 1.47(1.45–1.49) \times 10^{-2}$ ($\chi^2$/d.o.f. = 552.8/426), where $z = 0.451$ and $N_{\rm H} = 4.85 \times 10^{20}$ cm$^{-2}$ are adopted. In comparison with the best-fit XIS parameters (Table 2), the temperature and the normalization are higher by about 1.5 keV and 7% for the *Chandra* data. We discuss below the possible reasons for these differences in the light of the *Suzaku* and *Chandra* calibration uncertainties.

1. *Suzaku* XIS
   Since the spatial extent of X-ray emission from RX J1347.5–1145 is small compared with the PSF of *Suzaku*, it can be treated as a point source (we have confirmed that the spectral fit with an auxiliary file generated for a point source at the HXD-nominal position yields spectral parameters statistically consistent with those listed in Table 2). According to the latest calibration of XIS and PIN, the best-fit power-law parameters describing the Crab spectra are the photon index $\Gamma = 2.073 \pm 0.006$ and the normalization $9.21 \pm 0.1$ photons cm$^{-2}$ s$^{-1}$ keV$^{-1}$, which are by about 1.5% and 5% lower than the "standard" values ($\Gamma = 2.10$, for the normalization = 9.7; Toor & Seward 1974).
   To simulate the effect of $\Gamma$, we multiplied the APEC model by the PLABS model, $E^{-\alpha}$, with $\alpha = -0.03$ and fitted this to the XIS+PIN spectra. The best-fit parameters were derived to be $kT = 11.85$ keV, $Z = 0.30$ solar, and $K = 1.35 \times 10^{-2}$ ($\chi^2$/d.o.f. = 1343/1219). This indicated that the *Suzaku* temperature measurement had a systematic error at the level of ~1 keV, although this then had the effect of increasing discrepancy between *Suzaku* and *Chandra* data results. The uncertainty in the *Suzaku* effective area is therefore unlikely to be a major source of the discrepancy.
2. *Chandra* ACIS-I
   Based on a comparison of cluster temperatures derived from *Chandra* and *XMM-Newton*, Snowden et al. (2008) reported that the *Chandra* temperature tends to be 1–2 keV higher than that of *XMM-Newton* particularly for clusters with $kT \gtrsim 5$ keV. Furthermore, the proceedings of the *Chandra*

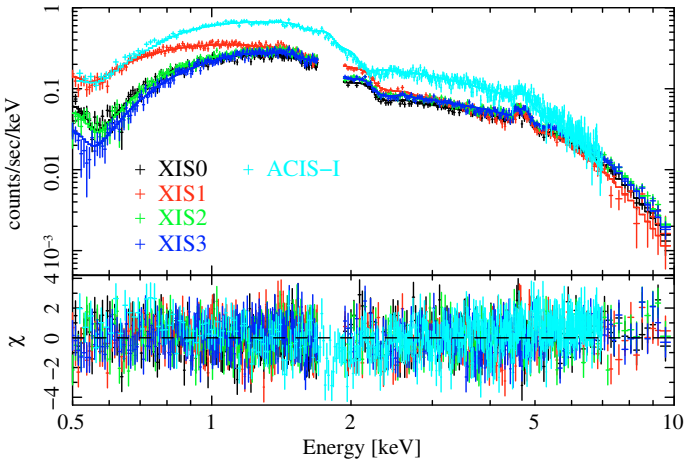


**Fig. A.1.** *Suzaku*/XIS+*Chandra*/ACIS-I spectra of RX J1347.5–1145 ($r < 5'$) simultaneously fitted with the APEC×PLABS model.

Calibration Workshop by David et al.[7] indicated the same tendency as well as that the temperature obtained from the fit to the 2–6 keV continuum spectra was systematically higher by about 2 keV than that inferred from the iron line ratios for hot clusters. We consider therefore the above results to suggest that the *Chandra* effective area has a systematic error at the level of $\Delta kT = +1 \sim +2$ keV for hot ($kT \gtrsim 5$ keV) clusters.

For example, fitting the *Chandra* data with the APEC model multiplied by the $\alpha = -0.03$ PLABS model leads to $kT = 12.89$ keV, $Z = 0.40$ solar, and $K = 1.44 \times 10^{-2}$ ($\chi^2$/d.o.f. $= 569/426$). Although the metal abundance is marginally higher, the temperature agrees with that of XIS.

By then simultaneously fitting the *Chandra* and XIS spectra with the APEC×PLABS model, we determined $\alpha$ and the relative normalization factor to be $-0.017(-0.031 \sim -0.003)$ and 1.07(1.06–1.08), respectively. The best-fit APEC parameters were $kT = 12.92$ keV, $Z = 0.35$ solar, and $K = 1.37 \times 10^{-2}$ ($\chi^2$/d.o.f. $= 1890/1636$). The result is plotted in Fig. A.1.

Based on the above discussion, to take into account the difference in the calibration of the two satellites, we assumed in Sect. 5 a *Chandra* normalization factor relative to XIS of $1/1.07 = 0.93$ and multiplied the spectral model derived with *Chandra* by the PLABS model with $\alpha = 0.02(0–0.03)$.

[7] http://cxc.harvard.edu/ccw/proceedings/07_proc/presentations/david/

## References


Allen, S. W., Schmidt, R. W., & Fabian, A. C. 2002, MNRAS, 335, 256
Anders, E., & Grevesse, N. 1989, Geochim. Cosmochim. Acta, 53, 197
Blumenthal, G. R., & Gould, R. J. 1970, Rev. Mod. Phys., 42, 237
Boldt, E. 1987, in Observational Cosmology, ed. A. Hewitt, G. Burbidge, & L. Z. Fang, IAU Symp. 124, 611
Bradač, M., Schrabback, T., Erben, T., et al. 2008, ApJ, 681, 187
Carter, J. A., & Read, A. M. 2007, A&A, 464, 1155
Cohen, J. G., & Kneib, J.-P. 2002, ApJ, 573, 524
Condon, J. J. 1974, ApJ, 188, 279
Dickey, J. M., & Lockman, F. J. 1990, ARA&A, 28, 215
Dunkley, J., Komatsu, E., Nolta, M. R., et al. 2008, ArXiv e-prints, 803
Ettori, S., Allen, S. W., & Fabian, A. C. 2001, MNRAS, 322, 187
Fischer, P., & Tyson, J. A. 1997, AJ, 114, 14
Frontera, F., Orlandini, M., Landi, R., et al. 2007, ApJ, 666, 86
Gitti, M., Ferrari, C., Domainko, W., Feretti, L., & Schindler, S. 2007a, A&A, 470, L25
Gitti, M., Piffaretti, R., & Schindler, S. 2007b, A&A, 472, 383
Halkola, A., Hildebrandt, H., Schrabback, T., et al. 2008, A&A, 481, 65
Ishisaki, Y., Maeda, Y., Fujimoto, R., et al. 2007, PASJ, 59, 113
Kawano, N., Fukazawa, Y., Nishino, S., et al. 2008, ArXiv e-prints, 805
Kitayama, T., Komatsu, E., Ota, N., et al. 2004, PASJ, 56, 17
Kokubun, M., Makishima, K., Takahashi, T., et al. 2007, PASJ, 59, 53
Komatsu, E., Kitayama, T., Suto, Y., et al. 1999, ApJ, 516, L1
Komatsu, E., Matsuo, H., Kitayama, T., et al. 2001, PASJ, 53, 57
Komatsu, E., Dunkley, J., Nolta, M. R., et al. 2008, ArXiv e-prints, 803
Koyama, K., Tsunemi, H., Dotani, T., et al. 2007, PASJ, 59, 23
Kushino, A., Ishisaki, Y., Morita, U., et al. 2002, PASJ, 54, 327
Markevitch, M., Gonzalez, A. H., David, L., et al. 2002, ApJ, 567, L27
Masai, K. 1994, ApJ, 437, 770
Mastropietro, C., & Burkert, A. 2007, ArXiv e-prints, 711
Milosavljević, M., Koda, J., Nagai, D., Nakar, E., & Shapiro, P. R. 2007, ApJ, 661, L131
Miranda, M., Sereno, M., de Filippis, E., & Paolillo, M. 2008, MNRAS, 385, 511
Mitsuda, K., Bautz, M., Inoue, H., et al. 2007, PASJ, 59, 1
Nevalainen, J., Oosterbroek, T., Bonamente, M., & Colafrancesco, S. 2004, ApJ, 608, 166
Nusser, A. 2008, MNRAS, 384, 343
Ota, N., Fukazawa, Y., Fabian, A. C., et al. 2007, PASJ, 59, 351
Petrosian, V., Madejski, G., & Luli, K. 2006, ApJ, 652, 948
Rephaeli, Y., Gruber, D., & Arieli, Y. 2006, ApJ, 649, 673
Rephaeli, Y., Nevalainen, J., Ohashi, T., & Bykov, A. M. 2008, Space Sci. Rev., 16
Sahu, K. C., Shaw, R. A., Kaiser, M. E., et al. 1998, ApJ, 492, L125
Sarazin, C. L., & Kempner, J. C. 2000, ApJ, 533, 73
Schindler, S., Hattori, M., Neumann, D. M., & Boehringer, H. 1997, A&A, 317, 646
Serlemitsos, P. J., Soong, Y., Chan, K.-W., et al. 2007, PASJ, 59, 9
Snowden, S. L., Mushotzky, R. F., Kuntz, K. D., & Davis, D. S. 2008, A&A, 478, 615
Springel, V., & Farrar, G. R. 2007, MNRAS, 380, 911
Takahashi, T., Abe, K., Endo, M., et al. 2007, PASJ, 59, 35
Takahashi, T., Kelley, R., Mitsuda, K., et al. 2008, ArXiv e-prints, 807
Takizawa, M. 1999, ApJ, 520, 514
Toor, A., & Seward, F. D. 1974, AJ, 79, 995
Uchiyama, Y., Maeda, Y., Ebara, M., et al. 2008, PASJ, 60, 35